RICE UNIVERSITY

Reaction Rates and Transition States:
A New Perspective on an Old Problem

by

Paul Jay Ledbetter

A THESIS SUBMITTED
IN PARTIAL FULFILLMENT OF THE
REQUIREMENTS FOR THE DEGREE

Masters of Science

Approved, Thesis Committee:

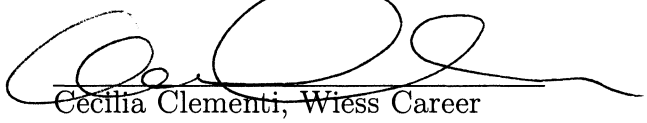

Cecilia Clementi, Wiess Career Development Chair, Professor of Chemistry, and Professor of Chemical and Biomolecular Engineering

Gustavo Scuseria, Robert A. Welch Professor of Chemistry, and Professor of Physics and Astronomy

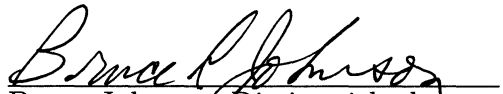

Bruce Johnson, Distinguished Faculty Fellow in Chemistry

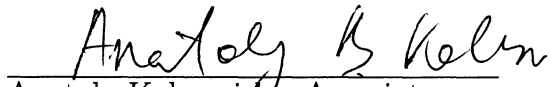

Anatoly Kolomeisky, Associate Professor of Chemistry, and Associate Professor of Chemical and Biomolecular Engineering

Houston, Texas
OCTOBER 2010

ABSTRACT

Reaction Rates and Transition States:A New Perspective on an Old Problem

by

Paul Jay Ledbetter

Transition state theory was originally developed in the 1930s as method for calculating chemical reaction rates in simple systems using energetic barrier heights. Unfortunately, its usefulness in complex high dimensional chemical processes such as protein dynamics is severely mitigated by the approximate assumption that reacting systems do not recross the transition state. This approximation has been improved for simple systems in modern variational transition state theory (VTST), which gives a close upper bound to the true reaction rate. For complex systems, location of the VTST separatrix is still theoretically challenging.

We propose the definition of an alternative transition state separatrix for systems with high friction which has the property that the escape rate through the separatrix gives the exact reaction rate for the system, without the need for recrossing corrections, and, surprisingly, without requiring the escaping trajectories to cross the reaction barrier.

However, locating this separatrix presently does require considering trajectories crossing the barrier. In order to lessen the computational challenge associated with barrier crossing, we provide an automatic method to enhance sampling of trajectories crossing the reaction barrier derived from the mathematics of super symmetry. This method provides an effective "ensemble magnifying glass," statistically inducing additional sampling of configurations in regions with large probability flux but without affecting transition rates.

Contents

Illustrations

Chapter 1

Introduction

As the building blocks of life, protein motions underlie all important bioengineering and medical problems. However, the complexity of these molecules pose important and challenging chemical problems which hinder their study. This places a high priority on the development of tools to allow researchers to both identify and characterize the mechanisms of protein behaviors. Among the chemical difficulties, is an apparent breakdown of chemical rate equations developed in the previous century. Even without the complexities of quantum chemical corrections which present problems in apparently simpler systems, we seem not to have escaped the problem Eyring believed he solved in the 1930s, namely, (without extensive simulation) we are only able to calculate relative rates of reactions in complex classical systems, not absolute rates.

As we summarize below, the suspected reasons for this breakdown in methods for calculating reaction rates is the difficulty of locating chemical transition states in a protein's high dimensional configuration space, and the failure of classical reaction rate equations to predict the reaction rates once the transition states are found. This is widely understood to be a consequence of the inability of the classical Transition State Theory (TST) to distinguish forward and backward reacting trajectories at equilibrium which prevent giving more than an unconstrained upper bound to reaction rates rather than the rates themselves.

The difference between the upper bound and the actual rate is partially mitigated in the use of Variational Transition State Theories (VTST), but it leaves a strong dependence on the coordinate system used to describe the reaction, and even with apparently good coordinates, the upper bound can still be orders of magnitude off

[9, 11].

One method proposed to help overcome these difficulties is Super Symmetric Molecular Dynamics (SuSyMD) [15, 14, 20]. A prescription for using SuSyMD to locate transition states was previously given by Mossa and Clementi[17], which was proposed to be able to locate both energetically and entropically dominated free energy barriers for reactions. However, investigations into this method showed that it failed to reliably locate states relevant to transition state theory, and it is argued conclusively in Section 3.1.4 that such a method could not identify purely entropic barriers.

In response, we have developed a new prescription for using SuSyMD presented in Section 3.1.3 which is capable of identifying both energetic and entropic free energy barriers, and demonstrate in terms of a new transition state theory (developed in Part 2), coupled with a generalized Kramer's escape rate formulation (Section 3.2) how it can be used identify the regions of configuration space which determine the reaction rate. As can be expected, this formulation of transition state theory still suffers from some of the same difficulties as classical TST; namely, the need to have detailed information about the configuration space energy surface and breakdowns of the quasi-equilibrium assumption. Fortunately, this is where the usefulness of SuSyMD becomes evident; it provides an automated means of enhancing the sampling of the regions of configuration space important to both our formulation of TST, and classical TST theories. Further testing is needed, but the initial theory and results show the combination of the two may be a powerful method for predicting reaction rates in complex chemical systems.

This thesis is organized as follows: In this first part we will briefly review current transition state theory and methods for computing reaction rates with comments on the source of problems in each. In Part 2, we presnt our new transition state theory, termed "χ_1 separtix theory", with applications in one-dimensional problems. In Part 3, we will present the new prescription for implementing and using SuSyMD,

describe the usefulness of SuSyMD for locating reaction barriers with application to two dimensional systems.

1.1 Transition State Theory

1.1.1 Classical Transition State Theory

Transiton state theory (TST) was originally developed in the 1930s as a mechanistic explanation of the empirical Arrhenius law for the reaction constant, $k = Ae^{-E_a/RT}$[22, 23]. Before classical TST, only the relative rates of reactions could be predicted due to the ambiguity of the Arrhenius factor A. In two body gas phase reactions, TST gave a mechanistic explanation for the Arrhenius factor and provided a means for accurate reaction rate prediction.

Classical TST assumes there is a separatrix between reactant and product states formed by the hypersurface of configurations near, and orthogonal to the unstable direction of the highest potential energy saddle point along the reaction path, termed the "transition state." By virtue of being composed of states the highest potential energy saddle point of the reaction, it is intuitively clear that the these comprised states are the most difficult to reach by the motion of the reactants, and therefore represent limiting step in the reaction. The rate at which particles on the transition state separatrix leave in the direction of the products per unit time v, is estimated in TST as the average forward velocity of particles crossing the transition state at equilibrium, $r = \int_F \exp\{-E/kT\}\,\bar{v}\,\mathrm{d}\sigma$, where the integral is evaluated over the states on the separatrix F with velocity in the direction of the product states. The actual population on the separatrix is estimated as the population of a quantum harmonic oscillator at equilibrium, n, giving the number of particles leaving the reactant region in unit time as nr. Then, the forward reaction rate for a reactant population n_A, should be $\frac{\mathrm{d}n_A}{\mathrm{d}t} = -nr$. Evaluating these integrals explicitly gives the form of the Arrhenius law with no unexplained terms.

In reality, the rate at which the reactant population decreases will be less than

this this rate, due in part to quantum uncertainty, friction and collisions with the environment. For the purposes of this thesis, we are interested in classical effects of friction and collision alone. In the case of friction and thermal noise, we note that the forward velocity of reactants is not conserved, and is quickly randomized by the collisions. In the case of high friction, the velocity distribution is still the Boltzmann distribution, but a large fraction of the population can be knocked back to the reactant state, significantly reducing the rate at which trajectories effectively leave the reactant population. Complex energy surfaces can greatly magnify the opportunity for recrossing to the reactant state.

1.1.2 Variational Transition State Theory

For diffusion limited systems, saddle points in the *energy* surface will have little relation to the chemical reaction rate. For example, there are no energy barriers in the in Van der Waals gas potential,

$$V_{\text{vdw}}(r) = \epsilon \left(\left(\frac{r_0}{r} \right)^{12} - 2 \left(\frac{r_0}{r} \right)^{6} \right). \tag{1.1}$$

However, there is a free energy barrier (Figure 1.1) and a reaction time.

Similarly, in Go-like coarse grained protein model[4], the energy is dominated by the non-local potential term

$$V_{\text{Go}} = \sum_{ij} \epsilon \left(\left(\frac{r_{0,ij}}{r_{ij}} \right)^{12} - 2\delta_{N(i,j)} \left(\frac{r_{0,ij}}{r_{ij}} \right)^{6} \right) \tag{1.2}$$

where the sum is over all the pairs of amino acid residues, and $\delta_{N(i,j)}$ means the attractive component of the VdW potential is present only between native contact pairs. Residues which are not destined to be in contact in the folded state exclude each other like non-attractive VdW gas particles, creating an entropic barrier. The back bone bonds represent relatively minor contribution to the energy profile compared to the non-local component because they remain nearly relaxed throughout the folding process. Because of the minimum frustration principle, Go-models tend

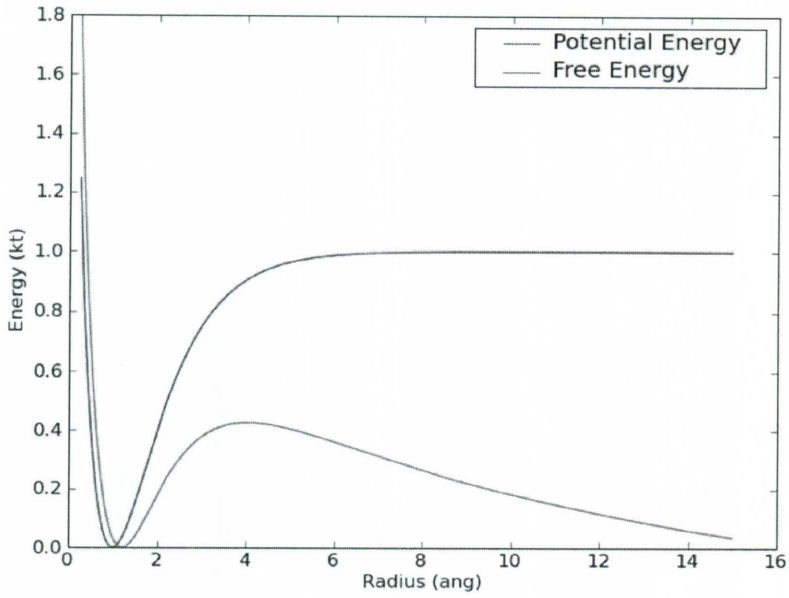

Figure 1.1 : Van der Waals energy and free energy. Although there is no potential energy barrier, there is a free energy barrier.

to give accurate characterization of dynamical protein folding behavior, despite the fact that the folding barrier is entirely entropic in these models.

The recrossing of reactant trajectories issue with classical TST is mitigated by the method first applied by Keck in 1960[12] which lead to Variational Transition State Theory(VTST). In the variational approach, Keck made use of the fact that, because the equilibrium flux through any separatrix dividing reactants and products gives an upper bound to the reaction rate, locating the dividing surface of least equilibrim flux will give the least TST upper bound to the reaction rate. Due to the assumption of thermodynamic equilibrium, the velocity distribution will be a Maxwell-Boltzmann distribution independent of the coordinate, and the surface of least flux becomes the surface of least spatial population density; or equivalently, the surface of minimal free energy along the reaction path. Keck gave particular examples by applying his technique to recombination reactions of gases which had small energy barriers and

more significant free energy barriers[12].

In complex reactions, this generalization of transition state theory has resulted in free energy saddle points being a focal point of investigation in complex reactions. However, as we will presently demonstrate, the search for saddle points in free energy is a difficult and ambiguous goal because the quantification of free energy depends on the collective coordinate used.

Given a full coordinate space $(x_1, ..., x_n)$ describing the configurations of a chemical system, we may define "collective" coordinates $(z_1, ..., z_m)$ for $m < n$, where each collective coordinate vector $\mathbf{z}$ corresponds to an $n - m$ dimensional *volume* of the full coordinate space. For example, we may map a two dimensional coordinate space $\mathbf{x} = (x_1, x_2)$, to the projection on a cartesian axis $z(\mathbf{x}) = x_1$.

Given collective coordinates, the free energy is

$$G(z) = -kT \ln \int_{z(x)=z} \exp\{-E(x)/kT\} \, \mathrm{d}^n x, \tag{1.3}$$

where the integral is taken over all x corresponding to the collective coordinate z. The appearance of free energy profile in z depends entirely on the collective coordinate used. For instance, in a full configuration space, $(z_i = x_i)$, the free energy is simply the energy, and saddle points in this free energy surface are just the saddle points of the energy surface.

A clear example for the effect of collective coordinate choice is given by the purely entropic barrier in two dimensions (Figure 1.2). Taking either of the two cartesian coordinates as collective variables leads to two radically different perspectives of the free energy profile (figures 1.3 and 1.4), one in which the relevant reaction barrier is a free energy minimum!

More extreme scenarios can be described, but the general conclusion is that any perturbation of the "ideal reaction coordinate" will lead to errors in the reaction rate. Complex reactions involving many degrees of freedom leave an arbitrarily large window for error in the perturbation of the ideal coordinate, leading to significant error.

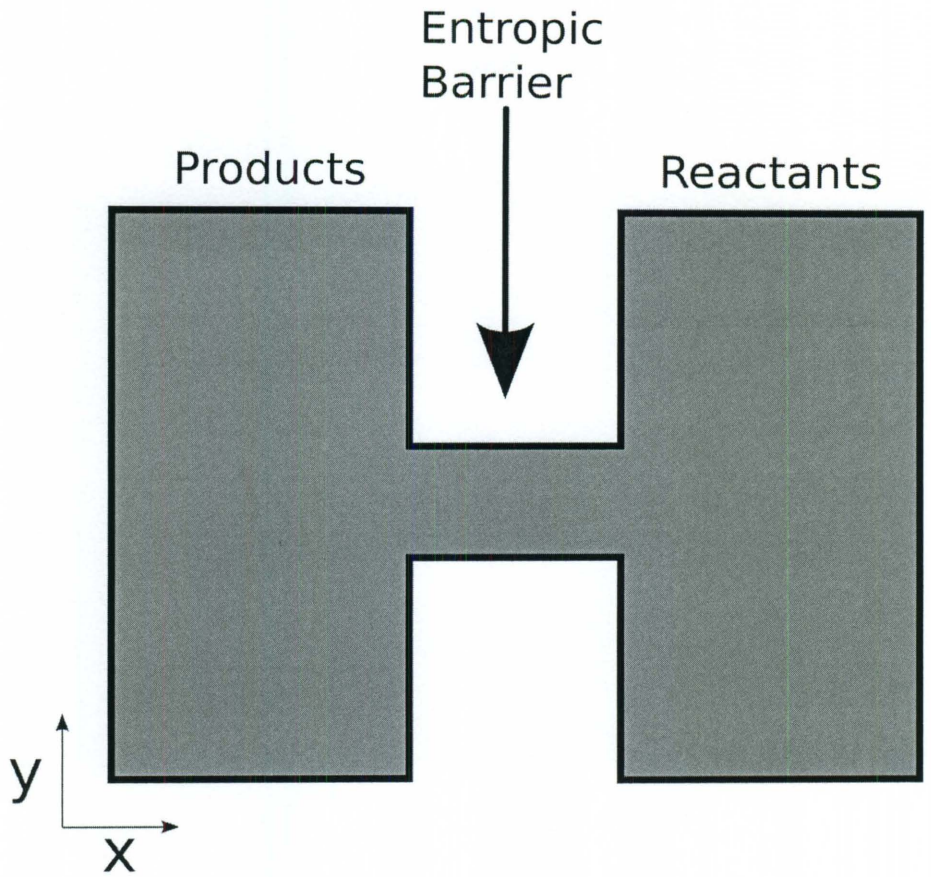

Figure 1.2 : An entropic barrier energy profile. The system is characterized by a region of zero forces surrounded by perfect reflecting walls.

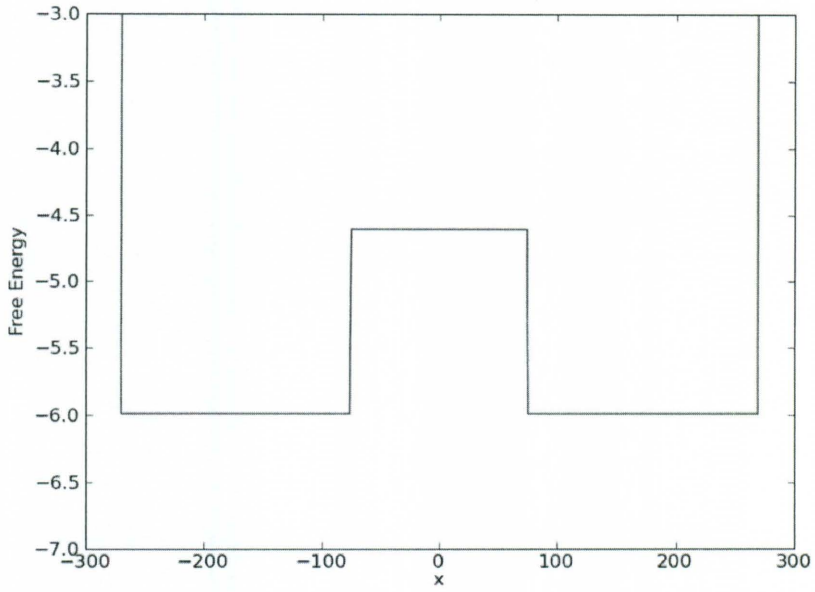

Figure 1.3 : The entropic barrier free energy profile along the collective coordinate x, $F(x) = -\ln \int \exp\{-E(x,y)\}\, \mathrm{d}y$. The reaction barrier is at $x = 0$.

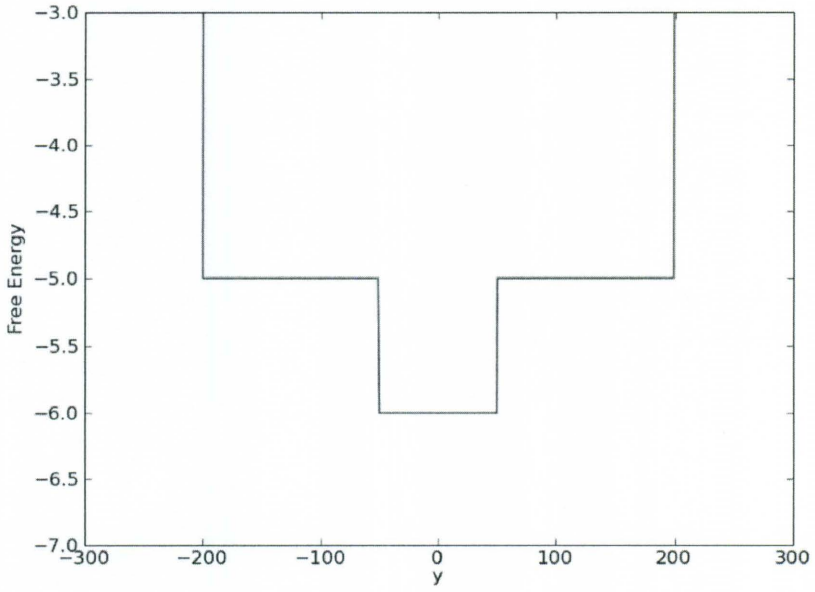

Figure 1.4 : The entropic barrier free energy profile along the collective coordinate y, $F(y) = -\ln \int \exp\{-E(x,y)\}\, \mathrm{d}x$. The reaction barrier is at $y = 0$.

1.1.3 p-fold Transition State

In the previous section, we noted that ideal reaction coordinates are necessary to give meaning to free energy profiles. In protein systems, the distortion of bad coordinates has led to suspicion of empirical folding coordinates and adoption by many of the dynamical coordinate p, and its accompanied transition state, the isocommitor surface [6, 7].

The p-fold coordinate is an intuitive measure of the kinetic distance of protein configurations from the folded and unfolded state. The basic idea is to perform multiple simulations starting from particular configurations and compute the relative probability p, of the protein reaching the folded state before the unfolded state. Clearly, p takes on a value of 1 near the folded state, and 0 near the unfolded state. The ensemble of configurations corresponding to $p = 0.5$ form the isocommitor surface, considered by many to be the relevant transition state for complex reactions.

While this coordinate indeed gives an intuitive measure of protein behavior and is considered by some researchers to be an "ideal coordinate by design," the direct connection to physical observables is not clear. There is no explicit relation between this transition state and reaction rates and "it is difficult to use it [p-fold] to characterize the system in a physically transparent manner."[6]. In comparison, even though empirical coordinates are suspect, they are directly related to physical observables, and there is contention that properly chosen structural empirical coordinates are adequate for free energy profiles in proteins [3].

Moreover, it is well noted that the isocommittor surface is practially impossible to measure experimentally[6, 3, 5]; it would involve repeatedly forcing a protein into, or finding a protein already in a specific highly improbable configuration; and tracking the individual protein to determine if it folds or unfolds first. Experimental methods for proteins have not yet reached this level of sophistication.

1.2 Fokker-Planck and Kramer's Equation

As we mentioned in Sections 1.1.1 and 1.1.2 a significant source of error in transition state theories is the neglect of transition state recrossings caused by friction. In 1940, Kramer gave an important supplement to TST by deriving the escape rate from a metastable state (the reactants) in diffusion systems, giving a correction to the forward reaction rate in TST compensating for friction[13].

In the following, we discuss the Kramer's equation (providing a basis for the Super Symmetric Kramer's Equation in Section 3.1) and give the derivation for the Kramer's escape rate in one dimensional systems. The motivation for discussing the escape rate in depth is two-fold: it will be used to verify the χ_1 transition state theory in one-dimensional examples in Section 2.2; and it will be used to explain the usefulness of Super Symmetric Molecular Dynamics in Section 3.2.

1.2.1 Kramer's Equation

It is well known that the dyanmics of a classical mechanical system can be described by the Hamilton equations of motion. Given the energy of the system in terms of the configuration coordinate q and the generalized momentum p, we write the energy of the system as $\mathcal{H}(q,p)$, and describe the time evolution of the classical state (q,p) by

$$\frac{\partial q}{\partial t} = \frac{\partial \mathcal{H}}{\partial p} = p \tag{1.4}$$

$$\frac{\partial p}{\partial t} = -\frac{\partial \mathcal{H}}{\partial q}. \tag{1.5}$$

In this thesis, we assume the configuration energy is conservative so that $\frac{\partial^2 \mathcal{H}}{\partial p \partial q} = 0$.

In principle, a complete classical system consisting of solvent and reactant particles could be integrated at once. However, in the thermodynamic limit, when the solvent is not a direct participant in the reaction, the solvent motion averages out and can be treated as a stochastic perturbation of the Hamilton equations. Then we can express the time dependence of the reactant alone using the Langevin equation at constant

temperature T

$$\begin{aligned} \frac{\partial q}{\partial t} &= p \\ \frac{\partial p}{\partial t} &= -\frac{\partial \mathcal{H}}{\partial q} - \gamma p + \sqrt{2T\gamma}\eta(t), \end{aligned} \tag{1.6}$$

where γ is the friction coefficient for the viscosity of the solvent, and $\eta(t)$ is a stochastic function with a standard normal distribution describing the random collisions with the solvent. The coefficient, $\sqrt{2T\gamma}$, on the stochastic component of the force is related to the fluctuation dissipation theorem, and ensures that the rate at which energy is removed from the system due to friction is compensated on average by the stochastic impulses so that a thermodynamic ensemble of such systems would evolve towards Maxwell-Boltzmann distribution with temperature T^*.

In protein systems where quantum effects can be neglected, integration of the Langevin equation gives accurate simulation of protein dynamics, and is the basis for many Molecular Dynamics(MD) techniques. In the MD simulations performed for this thesis, the Langevin equation for the relevant systems was integrated using a quasisymplectic integrator described by Manella[16].

By making use of the principles of Brownian motion (Langevin dynamics), Kramer integrated an ensemble of the trajectories for a differential increment of time giving the time evolution of the phase space density associated with a thermodynamic ensemble of Langevin trajectories.

We write Kramer's equation as

$$\frac{\partial}{\partial t}\psi = \mathbf{H}_{\mathrm{K}}\psi, \tag{1.7}$$

where the Kramer's operator is

$$\mathbf{H}_{\mathrm{K}} = -\gamma\frac{\partial}{\partial p_i}\left(T\frac{\partial}{\partial p_i} + \frac{\partial \mathcal{H}}{\partial p_i}\right) - \left(\frac{\partial \mathcal{H}}{\partial q_i}\frac{\partial}{\partial p_i} - \frac{\partial \mathcal{H}}{\partial p_i}\frac{\partial}{\partial q_i}\right). \tag{1.8}$$

*In the following we are using a temperature scale $k_b T = 1$.

This is the form of a divergence ($\left(\frac{\partial}{\partial q_i}, \frac{\partial}{\partial p_i}\right)$) of the the position and velocity currents,

$$J_{q_i} = \frac{\partial \mathcal{H}}{\partial p_i}\psi, \tag{1.9}$$
$$J_{p_i} = -\left(\gamma T \frac{\partial}{\partial p_i} + \gamma \frac{\partial \mathcal{H}}{\partial p_i} + \frac{\partial \mathcal{H}}{\partial q_i}\right)\psi.$$

1.2.2 Fokker-Planck Equation

In the moderate to high friction limit, where the timescale $1/\gamma$ is much smaller than relevant motions, the dependence of Kramer's equation on the generalized velocity can be neglected, yielding the simpler and theoretically more amenable Fokker-Planck equation. This was the equation Kramer used to determine the escape rate of particles from a metastable state. Fortunately, the approximations inherent in the Fokker-Planck equation are also the approximations generally considered representative for protein systems.

Dividing the force equation in Equation 1.6 by the friction constant γ, we obtain

$$\frac{1}{\gamma}\frac{\partial p}{\partial t} = -\frac{1}{\gamma}\frac{\partial H}{\partial q} - p + \sqrt{\frac{2T}{\gamma}}\eta(t) \tag{1.10}$$

In the high friction limit this is approximately zero, and we may effectively equate

$$p \approx -\frac{1}{\gamma}\frac{\partial H}{\partial q} + \sqrt{\frac{2T}{\gamma}}\eta(t) \tag{1.11}$$

Giving a time evolution for the configuration coordinate

$$\frac{\partial q}{\partial t} = -\frac{1}{\gamma}\frac{\partial H}{\partial q} + \sqrt{\frac{2T}{\gamma}}\eta(t), \tag{1.12}$$

independent of p.

Integration of the ensemble of trajectories as was done for Kramer's equation gives

$$\frac{\partial P}{\partial t} = \frac{\partial}{\partial q}\left(\frac{T}{\gamma}\frac{\partial}{\partial q} + \frac{1}{\gamma}\frac{\partial H}{\partial q}\right)P. \tag{1.13}$$

Rescaling the time to units of inverse friction, $t \rightarrow t/\gamma$, gives the simplified form

$$\frac{\partial P}{\partial t} = -\mathbf{H}_{\mathrm{FP}} P \tag{1.14}$$

where the Fokker-Planck operator is

$$\mathbf{H}_{\mathrm{FP}} = \frac{\partial}{\partial q}\left(T\frac{\partial}{\partial q} + \frac{\partial H}{\partial q}\right). \tag{1.15}$$

Equation 1.14 can be seen as a continuity relation for the probability distribution P and current

$$\mathbf{J} = \left(T\frac{\partial}{\partial q} + \frac{\partial H}{\partial q}\right) P. \tag{1.16}$$

1.2.3 Eigenfunctions and boundary conditions

The technique of separation of variables shows that the time dependent population densities for the Kramer's and Fokker-Planck equations may be written in terms of sum of the associated operator eigenvalues as

$$P(x,t) = \sum_i c_i \psi_i(x) e^{-\lambda_i t}. \tag{1.17}$$

for expansion coefficients c_i, eigenfunctions ψ_i and eigenvalues λ_i. From Equation 1.17 we can see clearly that the associated eigenfunctions represent particular displacements of the population from equilibrium which uniformly relax to equilibrium at the rate λ_i.

The Fokker-Planck and Kramer's operators are not Hermitian, so their eigenfunctions are not orthogonal, but are rather bi-orthogonal to their conjugate pairs:

$$\int e^{E\beta} \psi_i \psi_j \, \mathrm{d}x = \delta_{ij}, \tag{1.18}$$

In the Fokker-Planck case, the conjugate pairs are $e^{E(x)\beta}\psi_i(x)$; where $E(x)$ is the energy of configuration x. Using this, we can obtain the expansion coefficients for an initial population distribution $P(x,0)$ by integrating

$$c_i = \int e^{E(x)\beta} \psi_i(x) P(x,0) \, \mathrm{d}V \tag{1.19}$$

over the configuration space.

For the purpose of this thesis, we assume two possiblities for the chemical systems under consideration. The first possibility is that the system is simply closed so that that the energy $E(x) \to \infty$ and the population current density $\mathbf{J}(x) \to 0$ as $x \to \infty$. The consequence of the these boundary conditions is there are no eigenfunctions with eigenvalue $\lambda_i < 0$, and the only eigenfunction with $\lambda_i = 0$ is the Boltzmann population distribution, $\psi_0 = e^{E\beta}$. In the case of closed systems, eigenfunctions with eigenvalue $\lambda_i \neq 0$ always satisfy $\int \psi_i \, \mathrm{d}V = 0$, so that the total population is time independent.

$$N = \int P(x,t) \, \mathrm{d}V \propto \int e^{-E(x)\beta} \, \mathrm{d}V. \tag{1.20}$$

In order to model real systems, there is also, implicitly, the constraint on the expansion coefficients c_i so that

$$P(x,0) = \sum_i c_i \psi_i > 0 \text{ for all } x. \tag{1.21}$$

The second possibility for the boundary conditions we consider is that the system is closed at infinity, and that there is a local absorbing surface where $P(x) = 0$, but $\mathbf{J}(x) \neq 0$. In these cases, the Boltzmann population distribution does not satisfy the absorbing boundary conditions and the eigenfunction with $\lambda_i = 0$ is the null function $\psi_0(x) = 0$. Physically, this means that in the limit of infinite time all of the trajectories eventually cross the absorbing surface

As diffusion equations, both the Kramer's and Fokker-Planck equation resemble the Schrödinger equation

$$i\hbar \frac{\partial}{\partial t} \psi = \mathcal{H} \psi. \tag{1.22}$$

Whereas the eigenvalues associated with the Hamiltonian operator in the Schrödinger give the energies of the respective stationary states, the eigenvalues associated with the Kramer's and Fokker-Planck diffusion operators give the timescale for the relaxation of metastable states.

1.2.4 Kramer's Escape Rate

We follow a derivation similar to Kramer in the moderate to high friction cases similar to Risken's presentation[19].

In a chemical reaction $A \rightarrow B$, the population of reactants and products correspond to distinct domains of the configuration space. The population of reactants at a given time is then the integral over the reactant configuration space $n_A(t) = \int_A P(x,t)\,\mathrm{d}V$. A similar definition applies to the number of products $n_B = \int_B P(x,t)\,\mathrm{d}V$. The Fokker-Planck equation can be reduced to a one-dimensional diffusion equation along the reaction coordinate in terms of the Potential of Mean Force and a coordinate dependent diffusion coefficient. The diffusion coefficient itself can be made independent of the coordinate by appropriate transformation of of variables. We generalize the escape rate formula in a diffusion coefficient independent way in Section 3.2, but for now simply assume the diffusion coefficient is contant. The one variable system is

$$\frac{\partial P}{\partial t} = \frac{\partial}{\partial \chi}\left(\frac{\partial}{\partial \chi} + \frac{\partial E}{\partial \chi}\right) P. \tag{1.23}$$

Writing the inverse temperature as $\beta = 1/T$, we can write the Fokker-Planck current, Equation 1.16, for this one dimensional system as

$$S = -Te^{-E\beta}\frac{\partial}{\partial \chi}\left(e^{E\beta}P(\chi,t)\right) \tag{1.24}$$

To derive Kramer's escape rate, we asuume a one-way reaction corresponding to the potential of the kind depicted in Figure 1.5. We assume the time scale for escape is great enough that reactants within the well are distributed approximately as they would be in thermodynamic equilibrium, or quasi-equilibrium. Then the population can be described approximately by, $P(\chi,t) = P(\chi_{\min},t)e^{-(E(\chi)-E(\chi_{\min}))\beta}$, and the flux crossing the barrier between $\chi_{\min}$ and A will be nearly constant in space. The violation of these conditions is biggest source of error, as we will investigate in Section 2.2. Multiplying the constant current, Equation 1.24, by $e^{E\beta}$ and integrating between

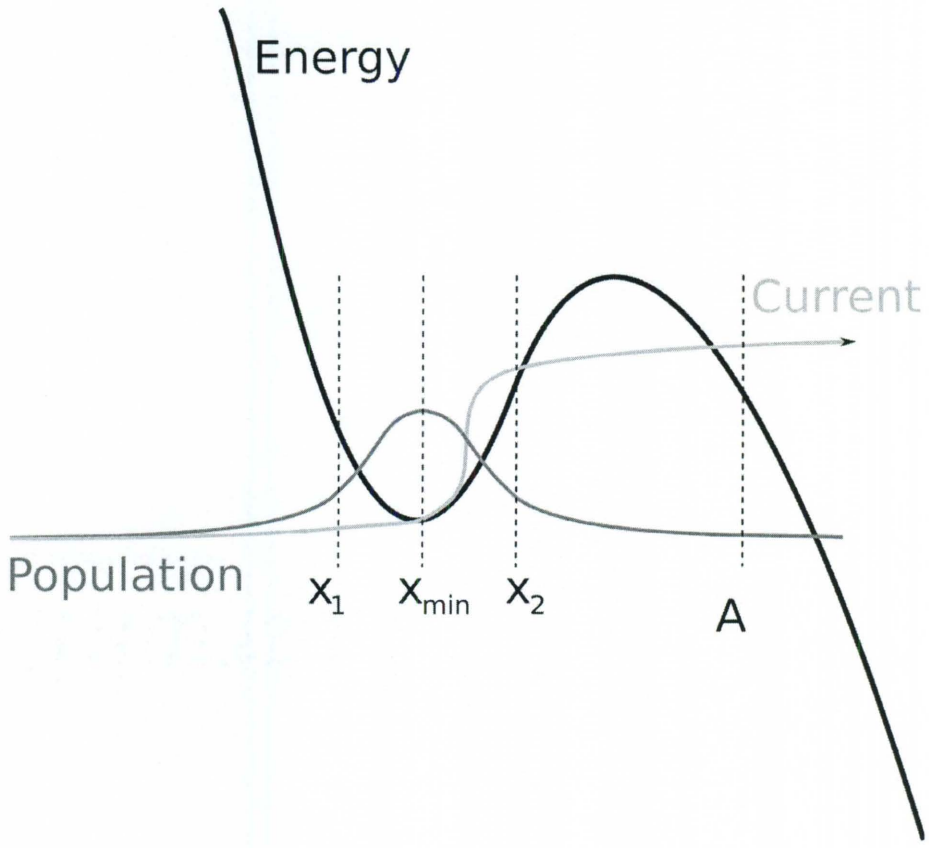

Figure 1.5 : Energy profile considered in Kramer's escape formula.

χ_{min} and A gives

$$S\int_{\chi_{\text{min}}}^{A} e^{E(\chi)\beta}\,\mathrm{d}\chi = T\left[e^{E(\chi_2)\beta}P(\chi_2,t) - e^{E(A)\beta}P(A,t)\right] \tag{1.25}$$

Because the particles escape at A, we may assume $P(A,t) = 0$, so the constant current is

$$S = \frac{Te^{E(\chi_{\text{min}})\beta}P(\chi_{\text{min}},t)}{\int_{\chi_{\text{min}}}^{A} e^{E(\chi)\beta}\,\mathrm{d}\chi} \tag{1.26}$$

The flux may also be written as the rate at which particles escape the well, λ, times the estimation of the total population in the well, $S = \lambda p$, where

$$p = \int_{\chi_1}^{\chi_2} P(x,t)\,\mathrm{d}x \approx P(\chi_{\text{min}},t)e^{E(\chi_{\text{min}})\beta}\int_{\chi_1}^{\chi_2} e^{-E(\chi)\beta}\,\mathrm{d}x. \tag{1.27}$$

Giving the inverse escape rate,

$$\frac{1}{\lambda} = \frac{p}{S} = \beta\left(\int_{\chi_{\text{min}}}^{A} e^{E(\chi)\beta}\,\mathrm{d}\chi\right)\left(\int_{\chi_1}^{\chi_2} e^{-E(\chi)\beta}\,\mathrm{d}\chi\right) \tag{1.28}$$

For smooth free energy functions, we can expand to second order at the top of the barrier, and the rate reduces to the classical TST rate with a friction dependent correction.

Many researchers have worked to increase the accuracy of this kind of general formula by increasing the accuracy of approximations based on local energetic information in general cases[18, 8]. However, while local energetic information may be sufficiently accurate in simple chemical systems, they can not be more accurate than the full integral calculation, which breaks down by itself for complex energetic surfaces.

Furthermore, Kramer's escape formula depends on the cancelation of the time dependent dependent population $P(\chi_{\text{min}},t)$ in Equation 1.28. This cancellation can only occur if the boundary of the volume of configuration space where the current is approximately constant is entirely enclosed in the volume of configuration space where the population is approximately a Boltzmann distribution, and vice-versa. In complex reactions, this assumption can not always be met.

Chapter 2

χ_1 Separatrix Theory

By studying the Fokker-Planck equation in quasi-equilibrium, we are able to give a mathematically precise definition for a transition state, termed the χ_1 separatrix, for chemical systems where the assumptions inherent in the Fokker-Planck equation (Equation 1.14) are appropriate. The χ_1 separatrix has the properties of being coordinate independent, and directly relatable to reaction rates and physical observables.

The intimate connection between the χ_1 separatrix and reaction rates is derived from the fact that accurate calculation of the escape rate to this separatrix gives the relaxation time for the reaction *regardless* of the complexity of the reaction. The connection between escape rates and relaxation times has been noted many times before in Mean First Passage Time approaches [18, 8, 2]. However, previous studies have focused on accurate escape rates over *barriers*, and did not note that choosing a particular generalized transition state connected to the global relaxation rate.

In this part, we define the χ_1 separatrix in Section 2.1 and compare it to the other transition states summarized in Part 1. In Section 2.2 the Kramer's escape rate formula from 1.2.4 is applied to calculate relaxation rates, and particular attention is given to the cases where Kramer's escape formula breaks down in reactions with intermediate minima.

2.1 Definition of χ_1 separatrix

To define the χ_1 separatrix, we suppose that the reactant and product configuration ensembles are the longest lived metastable states on the timescale of observation*. In Section 2.1.1, we show the assumption of reactants and products being the longest lived metastable state is equivalent to assuming that the time dependent decay of reactants can be written as a single exponential as in a reaction rate equation.

Under this condition, the χ_1 separatrix is the hypersurface described by the root of the first non-zero eigenfunction of the Fokker-Planck equation for the chemical system. In complex reactions where there are intermediates long lived on the timescale of the reaction, we can define additional χ_2 separatices, but for brevity we neglect these considerations since they do not affect the properties of the χ_1 separatrix.

2.1.1 Relation of χ_1 Separatrix to Reaction Rates

Forward and backward reaction rate constants can be related to χ_1 separatrix by writing the rates in terms of the Fokker-Planck equation. We write the rate at which which reactants are becoming products by v_F; and the rate at which products are becoming reactants by v_R. These rates are related to the number of reactants and products , n_A and n_B respectively, by the reaction rate constants, k_F and k_R by the relation

$$v_F = k_F n_A \text{ and } v_R = k_R n_B \tag{2.1}$$

The explicit value for the rate constants depend on the choice of the transition state separatrix due to the fact that the separatrix *defines* the reactant and product configuration volumes. However, the rate constants can be eliminated in favor of the

*In reality, it is inescapable that there will always be longer lived metastable states. We can really only assume that the timescale required to obtain a non-neglible population of states which are neither reactant or product is much longer than the time required for the reactant and product populations to relax to mutual equilibrium.

"relaxation rate", independent of the definition of the separatrix. To do this, we note that the time dependent concentrations obey

$$\frac{\mathrm{d}n_A}{\mathrm{d}t} = k_R n_B - k_F n_A, \tag{2.2}$$

$$\frac{\mathrm{d}n_B}{\mathrm{d}t} = -\frac{\mathrm{d}n_A}{\mathrm{d}t} \tag{2.3}$$

Representing the equilibrium number of particles by $n_{A=}$, and assuming an initial concentration $n_{A0} = n_{A=} + C$, and a relaxation rate λ, it's easy to verify that $n_A = n_{A=} + Ce^{-\lambda t}$, and $n_B = n_{B=} - Ce^{-\lambda t}$ satisfy the above differential equations as long as

$$k_F = \frac{\lambda n_{B=}}{n_{A=} + n_{B=}} \tag{2.4}$$

$$\text{and } k_R = \frac{\lambda n_{A=}}{n_{A=} + n_{B=}}. \tag{2.5}$$

Now, the relaxation rate can be related directly to the χ_1 separatrix, giving its relation to the forward and backward rate constants.

As we noted in Section 1.2.3, the time dependent solutions to the Fokker-Planck equation can be written in terms of its eigenfunctions as

$$P(x,t) = \psi_0(x) + c_1\psi_1(x)e^{-\lambda_1 t} + c_2\psi_2(x)e^{-\lambda_2 t} + \ldots \tag{2.6}$$

where ψ_0 is the Boltzmann distribution. For the present discussion we assume that the reactant and product populations are the longest are associated with the longest lived metastable states. Then, after a time $t > 1/\lambda_2$, the population can be represented effectively by

$$P(x,t) \approx \psi_0(x) + c_1 e^{-\lambda_1 t}\psi_1(x). \tag{2.7}$$

In other words, the Fokker-Planck solution behaves exactly as the equilibrating densities with the relaxation rate $\lambda = \lambda_1$ (which implies that the reaction rate equations are equivalent to the assumption of quasi-equilibrium in the Fokker-Planck diffusion). Therefore, calculating this value would allow us to determine the reaction rates at any separatrix.

To give a direct method for calculating the relaxation rate, we may consider the Fokker-Planck equation with an absorbing surface at the χ_1 separatrix. In other words, we look for solutions to the Fokker-Planck equation, $\mathbf{H}_{\mathrm{FP}}\psi = \lambda\psi$, constrained to the domain contained within the volume surrounded by $\psi_1(x)$, with the boundary condition $\psi(x) = 0$ when $\psi_1(x) = 0$. Effectively, this condition is equivalent to removing trajectories when they cross the separatrix (i.e., removing products as they form).

The boundary condition prevents the Boltzmann equilibrium from being a solution, and leads to the zero-eigenvalue solution being the null function. In other words, in the infinite time limit, the number of particles goes to zero because they all eventually cross the separatrix. Additionally, we see that $\psi_1(x)$ restricted to this domain is trivially a solution to the Fokker-Planck equation with the absorbing boundary; and since it has no roots within this domain, it is the lowest non-zero eigenfunction. Then, after a time $t > 1/\lambda_2$, approaching quasi-equilibrium in this system, the total number of particles at any time is $n_A = \int c_1\psi_1(x)e^{-\lambda_1 t}\,\mathrm{d}V$, and the rate at which particles escape the system satisfies

$$\frac{1}{n_A}\frac{\mathrm{d}n_A}{\mathrm{d}t} = -\lambda_1. \tag{2.8}$$

Note that if the bounding separatrix were changed, ψ_1 would no longer be the lowest non-zero eigenfunction, and in the escape rate would be different. Thus, in order to calculate the relaxation rate exactly, as opposed to bounding them, the separatrix where $\psi_1(x) = 0$ must be used.

Equivalently, we could consider the original system in quasi-equilibrium, and observe the net flux through the separatrix. Using the Fokker-Planck current operator

$\mathcal{J} = -\hat{x}_i(T\frac{\partial}{\partial x_i} + \frac{\partial E}{\partial x_i})$.

$$\int \mathcal{J}P(x,t) \cdot \mathrm{d}\sigma = \int_{\psi_1<0} \mathbf{H}_{\mathrm{FP}} P(x,t)\,\mathrm{d}V \tag{2.9}$$

$$= \int_{\psi_1<0} \frac{\partial}{\partial t} P(x,t)\,\mathrm{d}V \tag{2.10}$$

$$= \frac{\partial}{\partial t} \int_{\psi_1<0} P(x,t)\,\mathrm{d}V \tag{2.11}$$

$$= \frac{\partial n_A}{\partial t}, \tag{2.12}$$

where $n_A = \int_{\psi_1<0} P(x,t)\,\mathrm{d}V$ by definition for this separatrix.

2.1.2 Properites of χ_1 Separatrix

Steady State Approximation and Experimental Observability

The transition state is characterized by a stationary population distribution in quasi-equilibrium. This is related to the steady-state assumption in chemical theory, where the population of "transition state" is considered to be constant in time. This assumption is sometimes considered an approximation and that in reality population of the transition state decays to equilibrium much faster than the reactants and products. In quasi-equilibrium, where the total population of reactants and products have relaxed to near equilibrium, the difference from the equilibrium population becomes neglible.

Writing the solution to the Fokker-Planck equation in terms of the two lowest non-vanishing eigenvalues:

$$P(x,t) = \psi_0(x) + c_1 e^{-\lambda_1 t}\psi_1(x) + c_2 e^{-\lambda_2 t}\psi_2(x) + \ldots \tag{2.13}$$

Starting from any initial condition, after waiting a time $t \gg 1/\lambda_2$, the population at the χ_1 separatrix is

$$P(x,t) = \psi_0(x) + c_2 e^{-\lambda_2 t}\psi_2(x) \approx \psi_0(x). \tag{2.14}$$

That is, the population at the χ_1 separatrix agrees with the equilibrium population on the order of e^{-x}, for $x \gg 1$.

It is plausible that this property of the separatrix could be observed experimentally: if some property distinguishing configurations of χ_1 can be identified (e.g., by the distance between two particular amino acids), then observation of the time independence of the population in a chemical reaction out of equilibrium would confirm its location in the configuration space. Alternatively, if the configurations corresponding to a stationary density were observed experimentally first, then this knowledge could be used in computational studies without requiring the separatrix to be found by simulation first.

Surface of Minimum Recrossing

The χ_1 separatrix also possesses the property of being the surface of minimum recrossing in a chemical reaction. The immediate consequence of this property is that the quasi-equilibrium flux through this surface is the same regardless of whether trajectories are removed immediately upon crossing it, as we used in Section 2.1.1.

This property is nominally similar to the property of the Varitional Transition State Theory (VTST) transition state. However, the VTST transtion state is the surface of *locally* minimum recrossing, whereas the χ_1 separatrix is the surface of globally minimum rerossing. Even though the transition state separatrix by definition divides the reactants and products, the locally minimum recrossing assumption requires additional putative, but undefined surfaces enclosing the reactant and product densities as depicted in Figure 2.1. Without the additional reactant and product surfaces, it would not be possible for a *forward* reacting trajectory to recross the transition state, since by definition it has reacted upon the first crossing. With the assumption that the product surface exists somewhere beyond the VTST transition state, it becomes possible to say that the "true" reactive flux is less than the flux through the VTST transition state.

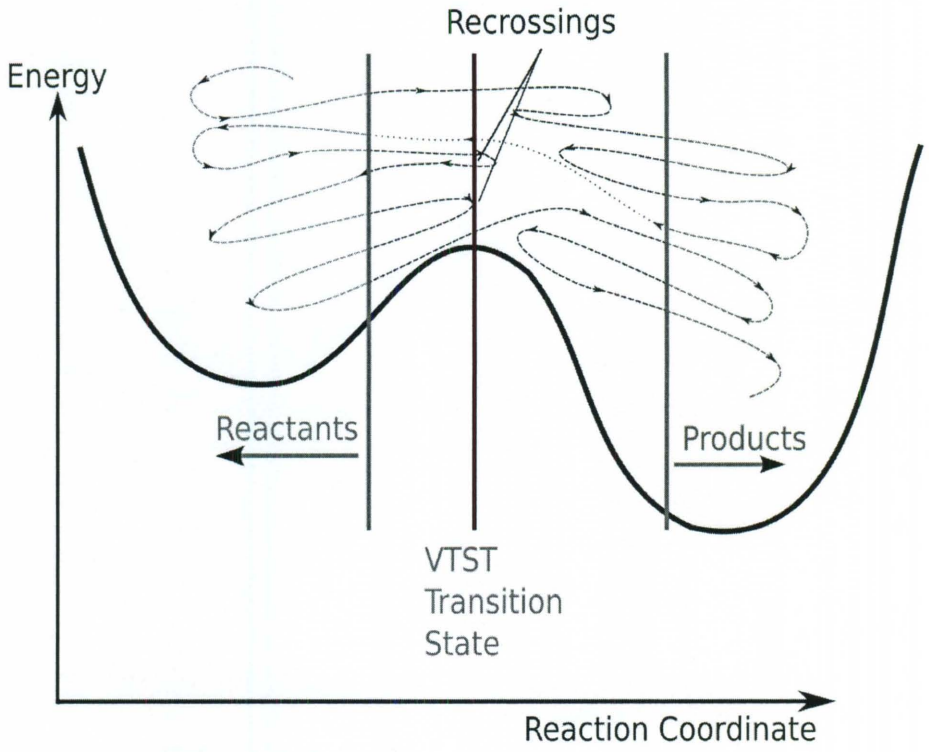

Figure 2.1 : The Variational Transition State Theory (VTST) separatrix is the locally minimum recrossing surface. The "local" assumption requires the existence of additional putative, but undefined surfaces enclosing the reactant and product densities. These additional surfaces introduce the possibility for a reactant trajectory to recross the transition state *on the way to product states* before finally reacting.

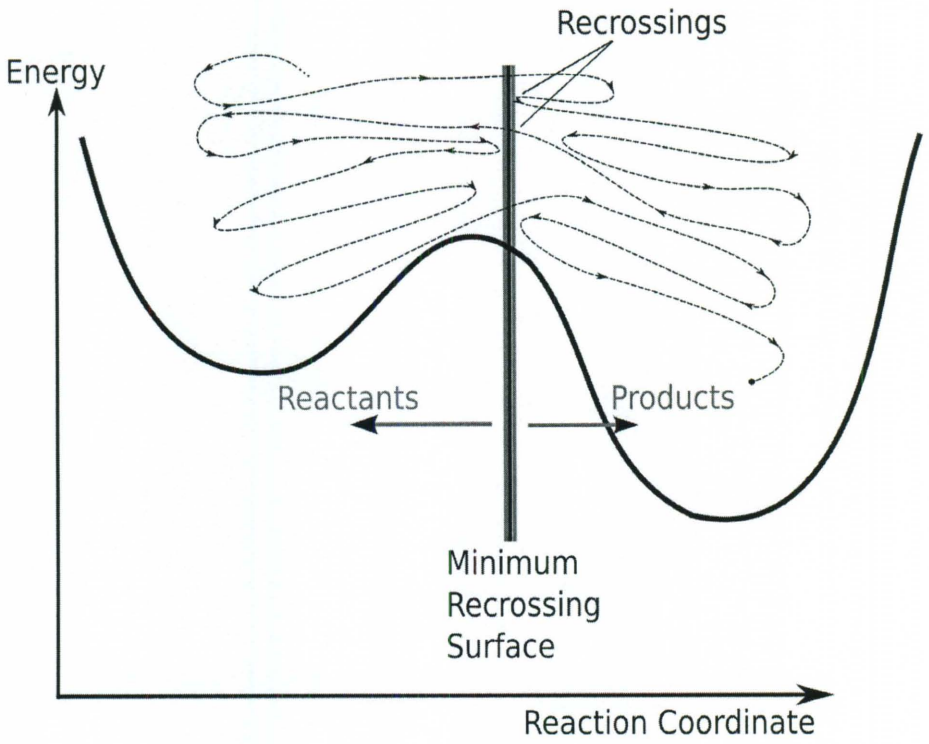

Figure 2.2 : Recrossing of the χ_1 separatrix. The χ_1 separatrix is the surface of minimum recrossing without definining additional ersatz reactant and product surfaces.

The χ_1 separatrix is the surface of minimum recrossing under the assumption that there is a constant flux of trajectories toward the product states, and that any crossing of the surface from the product side is a recrossing as depicted in Figure 2.2.

To demonstrate this property, we assume there is a constant non-equilibrium flow of reacting trajectories toward the separatrix; and by this assumption any reverse flux would partially cancel the one way reacting flux, reducing the net flux. For instance, the continuous circulation of trajectories in the reactant well would gives a near complete annihilation of the net flux through any surface in that region.

As such, we can identify the minimum recrossing surface by finding the surface of maximum net flux in quasi-equilibrim (as in Equation 2.7, $P(x,t) \approx \psi_0(x) + c_1 e^{-\lambda_1 t}\psi_1(x)$). We index all possible surfaces by χ, and denote their respective surfaces

by $\partial\chi$ and the enclosed volumes by $|\partial\chi|$. Then the surface of maximal net flux is:

$$\text{maxarg}_\chi \int_{\partial\chi} \mathbf{J}(\mathbf{x}) \cdot \mathrm{d}\sigma = \text{maxarg}_\chi \int_{|\partial\chi|} \nabla \cdot \mathbf{J}(\mathbf{x})\, \mathrm{d}V \tag{2.15}$$

$$= \text{maxarg}_\chi \int_{|\partial\chi|} \frac{\partial P}{\partial t}\, \mathrm{d}V = \text{maxarg}_\chi \int_{|\partial\chi|} c_1\psi_1(x)\frac{\partial e^{-\lambda t}}{\partial t}\, \mathrm{d}V \tag{2.16}$$

The expansion coefficient and are independent of χ and do not affect the maximiation

$$= \text{maxarg}_\chi \int_{|\partial\chi|} \psi_1(x)\, \mathrm{d}V \tag{2.17}$$

$$\tag{2.18}$$

Now, we can partition the subvolumes into $|\partial\chi|_+ = \{x | x \in |\partial\chi| \text{ and } \psi_1(x) > 0\}$ and $|\partial\chi|_- = \{x | x \in |\partial\chi| \text{ and } \psi_1(x) < 0\}$. And note that

$$\int_{|\partial\chi|} \psi_1(x)\, \mathrm{d}V = \int_{|\partial\chi|_+} \psi_1(x)\, \mathrm{d}V + \int_{|\partial\chi|_-} \psi_1(x)\, \mathrm{d}V \tag{2.19}$$

$$\leq \int_{|\partial\chi|_+} \psi_1(x)\, \mathrm{d}V \leq \int_{V_+} \psi_1(x)\, \mathrm{d}V \tag{2.20}$$

where the volume $V_+ = \{x | \psi_1(x) > 0\}$. Hence, the dividing surface, $\text{maxarg}_\chi \int_{\partial\chi} \mathbf{J}(\mathbf{x}) \cdot \mathrm{d}\sigma$ is the surface where $\psi_1(x) = 0$, the χ_1 separatrix.

Comparison to p-fold

As with the transition state of Variational Transition State Theory, the χ_1 separatrix also bears a resemblance to the isocommitor transition state of the p-fold coordinate (described in Section 1.1.3), due to the time indepedent probability density at quasi-equilibrium. Because the isocommitor surface has equal probability of going to the reactant or product, and the time independent population of the χ_1 separatrix is maintained by equal flux from the reactant and product, cursory might suspect they are the same surface. However this is not the case, as we will demonstrate by considering transtion rates.

We write write the probability, for a configuration in state x_i at time t_1 to be found in state x_j at time t_2 as $T(x_i, x_j; t_1, t_2)$. We are interested in a time-independent

property, so we neglect writing t_1 and t_2 explicitly, and write simply $T(x_i, x_j)$. The stationary density condition implies that for any x_1 on the χ_1 separatrix,

$$\int T(x, x_1) \left(\psi_0(x) + c_1\psi_1(x)\right) \, \mathrm{d}x = \int T(x_1, x) \left(\psi_0(x_1) + c_1\psi_1(x_1)\right) \, \mathrm{d}x$$

because we assume $\psi_1(x_1) = 0$, this simplifies to

$$= \int T(x_1, x)\psi_0(x_1) \, \mathrm{d}x. \tag{2.21}$$

The condition of detailed balance (which is elaborated in Section 3.1.4) tells us

$$T(x, x_1)\psi_0(x) = T(x_1, x)\psi_0(x_1). \tag{2.22}$$

Subsitution of the detailed balance condition into 2.21 eliminates ψ_0 , giving

$$\int T(x, x_1)\psi_1(x) \, \mathrm{d}x = 0. \tag{2.23}$$

We can partition the integral in Equation 2.23 into regions over the reactant states R, defined by the regions where $\psi_1(x) > 0$, and product states P where $\psi_1(x) < 0$, giving

$$\int_P T(x, x_1) \left|\psi_1(x)\right| \, \mathrm{d}x = \int_R T(x, x_1) \left|\psi_1(x)\right| \, \mathrm{d}x. \tag{2.24}$$

Equation 2.24 gives a requisite condition for x_1 to be on the χ_1 separatrix.

We may give a similar requisite for a point x_1 to be on the isocommitor surface. When working with p-fold rates, one usually defines reactant and product surfaces, ∂R and ∂P respectively, depending on intuition about the reactant and product states. The isocommitor surface is then defined by the points for which the transition rate to the enclosed reactant volume R is equal to the transition rate to the enclosed product volume P :

$$\int_P T(x, x_1) \, \mathrm{d}x = \int_R T(x, x_1) \, \mathrm{d}x. \tag{2.25}$$

While markedly similar, equations 2.24 and 2.25 are not in general the same, due to the fact that Equation 2.24 implicitly considers the global behavior of the reaction by way of the distribution of ψ_1 in space.

2.2 Kramer's escape rate in the context of χ_1 separatrix theory

As shown in Section 2.1.1, the problem of calculating the relaxation time for a chemical reaction can be reduced to the problem of finding the escape rate from either the reactant or product states to the χ_1 separatrix. The relation between escape rates and relaxation time has been recognized before, however previous authors have focused, as Kramer did, on giving approximations for the escape rate in the case of a single dominant barrier and did not point out the significance of the χ_1 separatrix, namely that it is the only surface for which the escape time gives the relaxation time for the complete reaction, as opposed to the relaxation time for the nearest barrier. And few differentiate between the relaxation rate and the forward reaction rate in a one-way reaction. Without considering the escape rate to the χ_1 separatrix explicitly, calculation of the escape rate in one direction can only be used as a dynamical correction to the approximation for the forward reaction of classical TST. Furthermore, the escape rate problem for diffusion systems is well studied in simple systems[8]. However,

In Part 3, we present Super Symmetric Molecular Dynamics as a tool for automatically enhancing the collection of the additional information needed to perform an accurate escape rate calculation.

We developed the Kramer's escape formula in Section 1.2.4, and observed that it was accurate only as long as the surface of the configuration volume of constant flux enclosed the surface configuration volume of quasi-equilibrium. The validity of this assumption is explored numerically in specific one-dimensional systems in Section 2.2.1.

The results show that in cases where either the reactant or product configuration space can be characterized by a single dominant barrier, the relaxation time for the entire reaction may be computed accurately.

2.2.1 Application of Escape Rate to One-Dimensional Systems

Method for computing χ_1 separatrix in one-dimension

In order to solve for the χ_1 separatrix numerically, we must find the root of the eigenfunction of the first non-vanishing eigenvalue. We solved for the eigenfunction by computing the eigenvectors of a matrix approximation for the Fokker-Planck operator, (Equation 1.15)

$$\mathbf{H}_{\mathrm{FP}} = \frac{\partial}{\partial q}\left(T\frac{\partial}{\partial q} + \frac{\partial H}{\partial q}\right). \tag{2.26}$$

The basis for the eigenvector space was chosen as dense set of Gaussians. Given a function $f(x)$ and a set of Gaussians centered at $\mu_1, ..., \mu_n$,

$$G(\alpha_i, \mu_i; x) = \exp\left\{-\alpha_i(\mu_i - x)^2\right\} \tag{2.27}$$

there exist interpolation coefficients, $c_1, ..., c_n$ such that

$$f(x) \approx \sum_j c_j G(\alpha_j, \mu_j; x). \tag{2.28}$$

The equality is exact at the Gaussian centers if coefficients are obtained from the linear system

$$f(\mu_i) = \sum_j c_j G(\alpha_j, \mu_j; \mu_i). \tag{2.29}$$

With the number of unknowns equal to the number of equations, there is always a single solution. For a given continuous operator $\hat{O}$ acting on the function space, there exists a matrix $\mathbf{O}$ such that

$$\{\hat{O}f\}(x) \approx \sum_k \left(\sum_j \mathbf{O}_{kj} c_j\right) G(\alpha_j, \mu_j; x) \tag{2.30}$$

Writing $G(\alpha_j, \mu_j; x)$ as $G_j(x)$ and expanding f, we see $\mathbf{O}$ must satisfy

$$\{\hat{O}f\}(x) \approx \sum_j c_j \{\hat{O}G_j\}(x) = \sum_j \left(\sum_k \mathbf{O}_{jk} c_k\right) G(\alpha_j, \mu_j; x) \tag{2.31}$$

$$= \sum_j c_j \sum_k \mathbf{O}_{kj} G(\alpha_j, \mu_j; x). \tag{2.32}$$

So the components of $\mathbf{O}$ can be determined by solving the tensor system

$$\{\hat{O}G_j\}(\mu_i) = \sum_k \mathbf{O}_{jk} G(\alpha_k, \mu_k; \mu_i). \tag{2.33}$$

Computation of the eigenvectors of the matrix for the Fokker-Planck operator gives interpolation coefficients for the associated eigenfunctions, allowing us to find the χ_1 separatrix at the root of ψ_1.

Measuring Breakdown In Kramer's Escape Assumptions

In Section 1.2.4, we observed the important assumption to the Kramer's escape formula was that there existed a point in the reactant region, $x_{\min}$, relative to which the quasi-equilibrium population inside $x_1 < x < x_2$ could be described as a Boltzman distribution; and the particle flux from $x_{\min}$ to the escape point A was constant.

We can quantify these assumptions in the following way. Given the quasi-equilibrium distribution in with absobring boundary conditions situation as being proportional to the eigenfunction with the least non-vanishing eigenvalue, $P(x,t) = c_1\psi_1(x)e^{-\lambda_1 t}$, we can compare the locally normalized (normalized within the well) quasi-equilibrium distribution to the locally normalized Boltzman distribution as:

$$\mathrm{Err}\left\{\psi_1 \propto e^{-E\beta}\right\}(x) = \frac{N_0}{e^{-E(x)\beta}}\left(\left|\frac{\psi_1(x)}{N_1}\right| - \frac{e^{-E\beta}}{N_0}\right), \tag{2.34}$$

where $N_0 = \int_{x_1}^{x_2} e^{-E(x)\beta}\,\mathrm{d}x$ and $N_1 = \int_{x_1}^{x_2} \psi_1(x)\,\mathrm{d}x$.

The break down in the constant flux condition can be quantified as

$$\mathrm{Err}\left\{\frac{\mathrm{d}J}{\mathrm{d}x} = 0\right\}(x) = \left|\frac{J_1(x) - J_1(A)}{J_1(A)}\right|, \tag{2.35}$$

where J_1 is the current of ψ_1 (Equation 1.16),

$$J_1(x) = \left(\frac{\partial}{\partial x} + \frac{\partial E}{\partial x}\right)\psi_1(x). \tag{2.36}$$

We may give an intuitive measure the mutual breakdown by

$$\{\text{Breakdown}\}(x) = \mathrm{Err}\{\frac{\mathrm{d}J}{\mathrm{d}x} = 0\}(x) + \left|\mathrm{Err}\{\psi_1 \propto e^{-E\beta}\}(x)\right| \tag{2.37}$$

These measures are used to study the breakdown of Kramer's assumptions in numerical solutions in sections 2.2.1 through 2.2.1. In particular, we find that Kramer's escape rate formula gives the most accurate results when $x_{\min}$ is chosen near the point of least mutual breakdown, and reasonable results are obtained as long as $x_{\min}$ is chosen near the reactant minima.

Calculation of Kramer's Escape Rate $\lambda_K(x)$

In most cases where Kramer's escape formula is used, it is assumed that the flux is over a symmetric barrier, allowing 1.28 to be approximated in terms of the curvature at the top of the barrier. However, the presence of an energy peak between $x_{\min}$ and A is not strictly necessary. In particular, we note that the necessary conditions are always approximated near the χ_1 separatrix, even though the χ_1 separatrix is not necessariy on the opposite side of a barrier. Furthermore, its important to note that in general, the approximations to Kramer's escape rate will necessarily be strictly less accurate than the full integral calculation of Equation 1.28.

In sections 2.2.1 through 2.2.1, we make use of the full integral approximation to study the accuracy of Kramer's integral for determining relaxtion rates using the χ_1 separatrix.

In these applications the choice for x_1 and x_2 are chosen based on an intuitive choices with minimal assumptions. For the escape from the left wells, we choose x_1 to be $-\infty$, and x_2 to be either the highest barrier, or the χ_1 separatrix, which ever is closer. Similarly, for the escape from the right well, we choose x_2 at ∞, and x_1 as the greater of the χ_1 separatrix and the highest barrier.

After choosing fixed x_1 and x_2, we calculate the Kramer's rate for different choices of $x_{\min}$, to assess the accuracy of the resulting rate compared to the breakdown of Kramer's assumptions described in the previous section, 2.2.1. This defines the

Kramer's rate for a given x from 1.28:

$$\lambda_K(x) = \left[\beta \left(\int_x^A e^{E(\chi)\beta}\, \mathrm{d}\chi\right) \left(\int_{\chi_1}^{\chi_2} e^{-E(\chi)\beta}\, \mathrm{d}\chi\right)\right]^{-1}. \tag{2.38}$$

External Barrier

In the following one dimensional systems, we use a common external barrier to create a closed system:

$$B(x) = kx^2 \left(1 - \exp\left\{-ax^2\right\}\right) \tag{2.39}$$

With a width $a = 1\mathrm{e} - 4$ and strength $k = 1.0, \mathrm{kT}$. This creates an energy profile which is neglible inside the region $-10. < x < 10.$ where we will vary the energy in each example, and rises smoothly to infinity as $x \to \pm\infty$. The energy of this barrier alone is depicted in Figure 2.3.

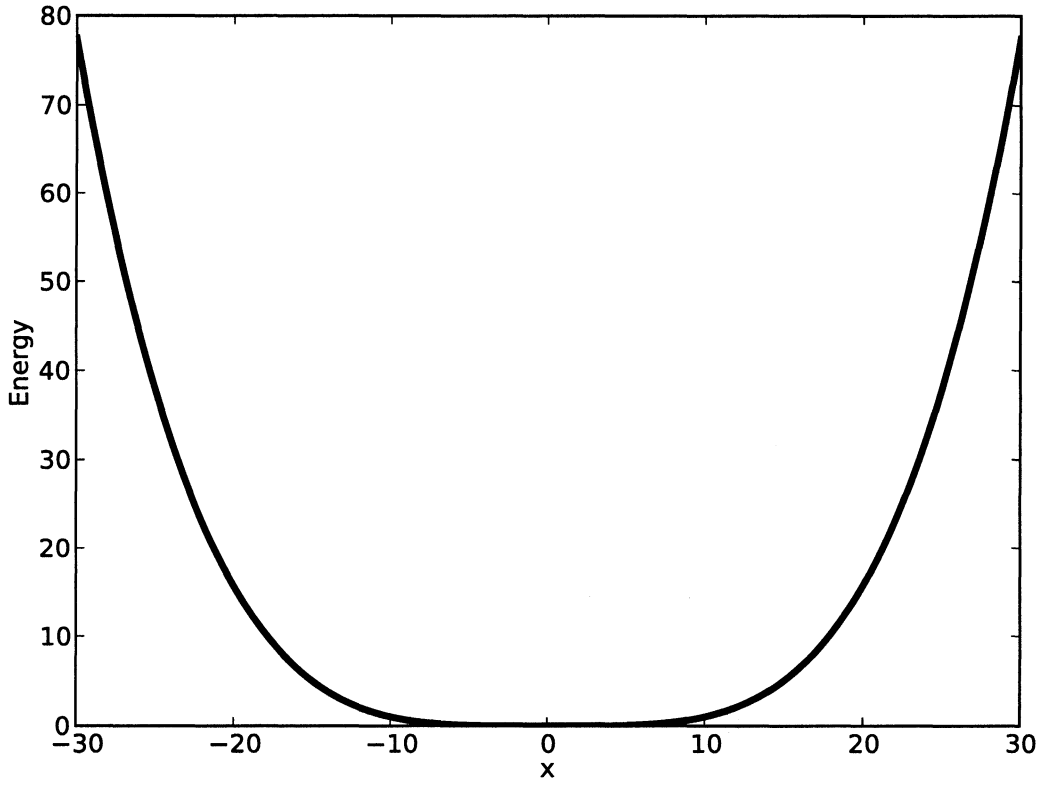

Figure 2.3 : Energy of the external Barrier Applied to One Dimensional Problems in sections 2.2.1 through 2.2.1.

Symmetric Single Barrier System

The simplest example for a one-dimensional system is the case of symmetric reactant and product energy profiles. We create an internal barrier

$$U_1(x) = k_1 \exp\left\{-a_1 x^2\right\}, \tag{2.40}$$

with strength $k_1 = 10., \mathrm{kT}$ and width $a_1 = 1\mathrm{e} - 2$. The composite system of the external barrier and symmetric internal barrier $V(x) = B(x) + U_1(x)$ is depicted in Figure 2.4.

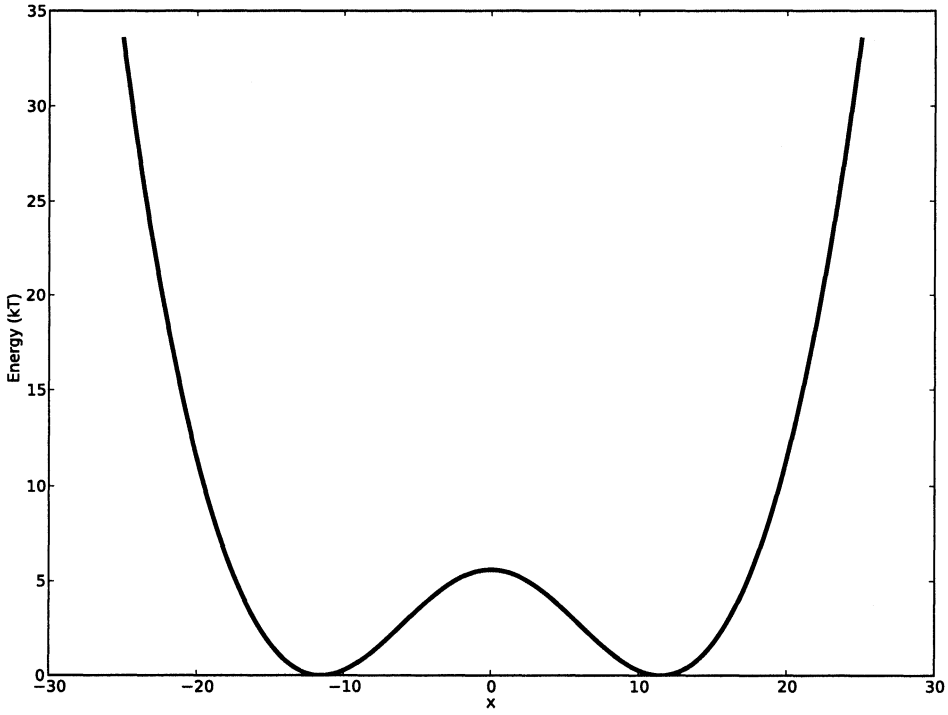

Figure 2.4 : The energy of the symmetric barrier potential $V(x) = B(x) + U_1(x)$, ($B(x)$ is given in Equation 2.39 and $U_1(x)$ in Equation 2.40)

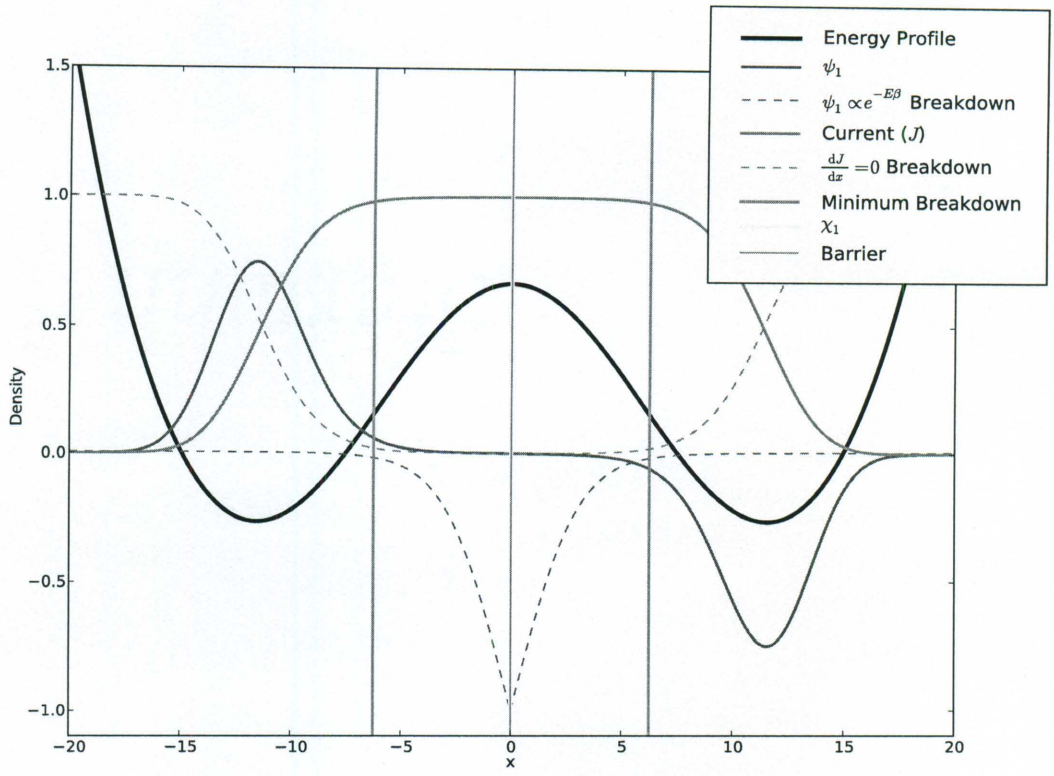

Figure 2.5 : The eigenfunction for the smallest non-vanishing eigenvalue, ψ_1, for the depicted energy profile; its associated current J, and the quantification of the breakdown in Kramer's assumptions as described in Section 2.2.1. The energy profile is provided for reference and is not to scale. The minimum mutual population and static current breakdowns, peak barrier and the χ_1 separatrix are indicated by vertical lines.

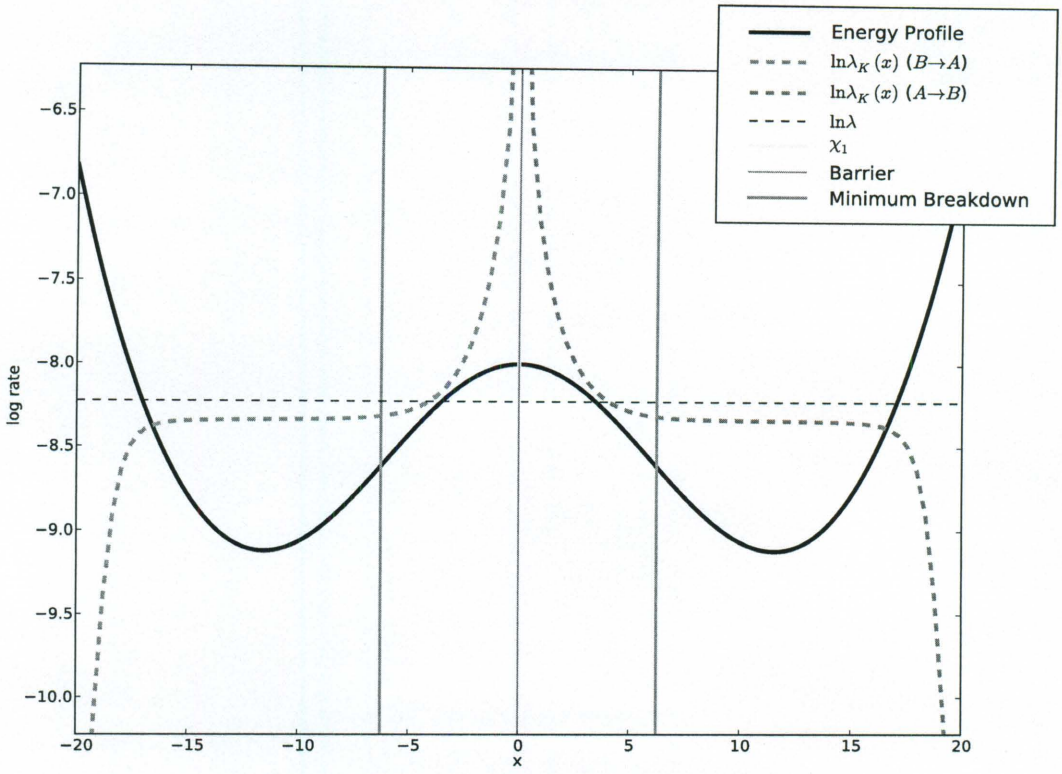

Figure 2.6 : The log of the reaction rates calculated by the escape Kramer's integral (Equation 1.28) for the depicted energy profile. The energy profile is provided for reference and is not to scale. The minimum mutual population and static current breakdowns, peak barrier and the χ_1 separatrix are indicated by vertical lines. The log of the reaction relaxation rate is indicated by a horizontal line.

Figure 2.7 : Symmetric Barrier Rates

Asymmetric Single Barrier System

In one-way, reactions, either the energy of the reactants or products are lower. We can give a simple example of such a potential by using an internal barrier of the form

$$U_2(x) = k_1 \exp\left\{-a_1(x-\mu_2)^2\right\}, \tag{2.41}$$

with strength $k_1 = 10., \mathrm{kT}$, width $a_1 = 1\mathrm{e}-2$, and center at and $\mu_2 = 4.0$. The composite system of the external barrier and symmetric internal barrier $V_2(x) = B(x) + U_2(x)$ is depicted in Figure 2.8.

We note the interesting property that the reaction rate can be calculated from the left well without crossing the barrier.

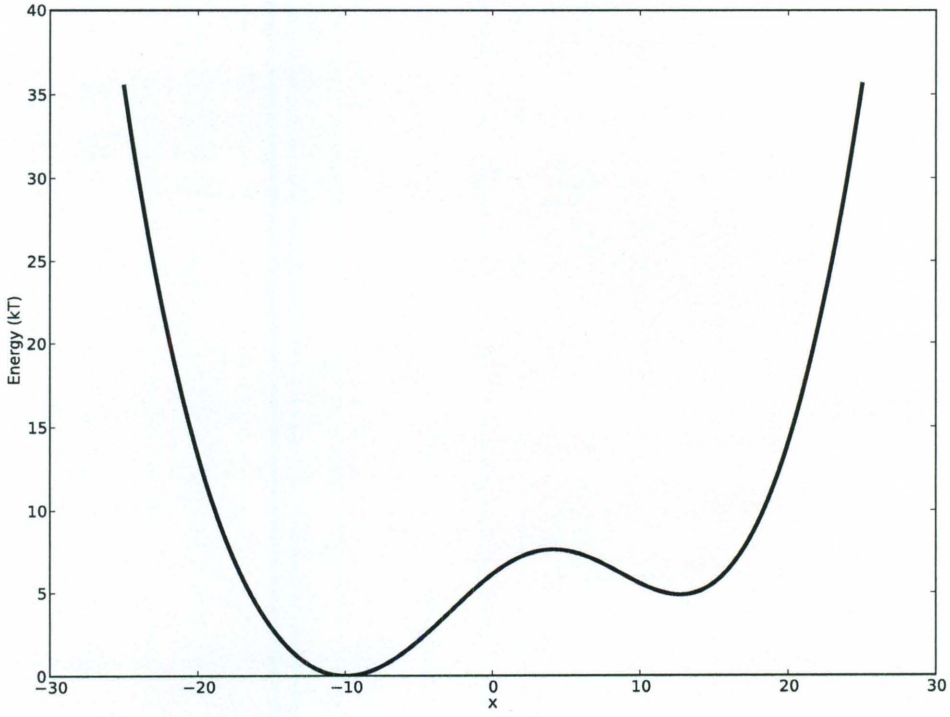

Figure 2.8 : The energy of the asymmetric barrier potential $V_2(x) = B(x) + U_2(x)$, ($B(x)$ is given in Equation 2.39 and $U_2(x)$ in Equation 2.41)

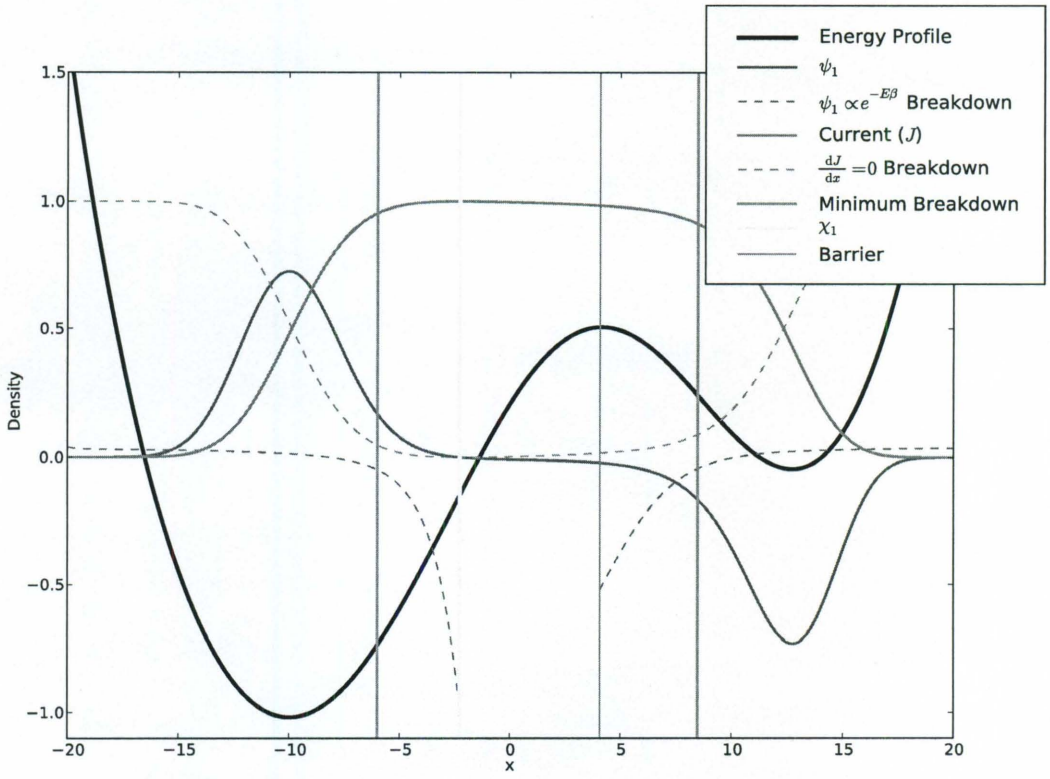

Figure 2.9 : The eigenfunction for the smallest non-vanishing eigenvalue, ψ_1, for the depicted energy profile; its associated current J, and the quantification of the breakdown in Kramer's assumptions as described in Section 2.2.1. The energy profile is provided for reference and is not to scale. The minimum mutual population and static current breakdowns, peak barrier and the χ_1 separatrix are indicated by vertical lines.

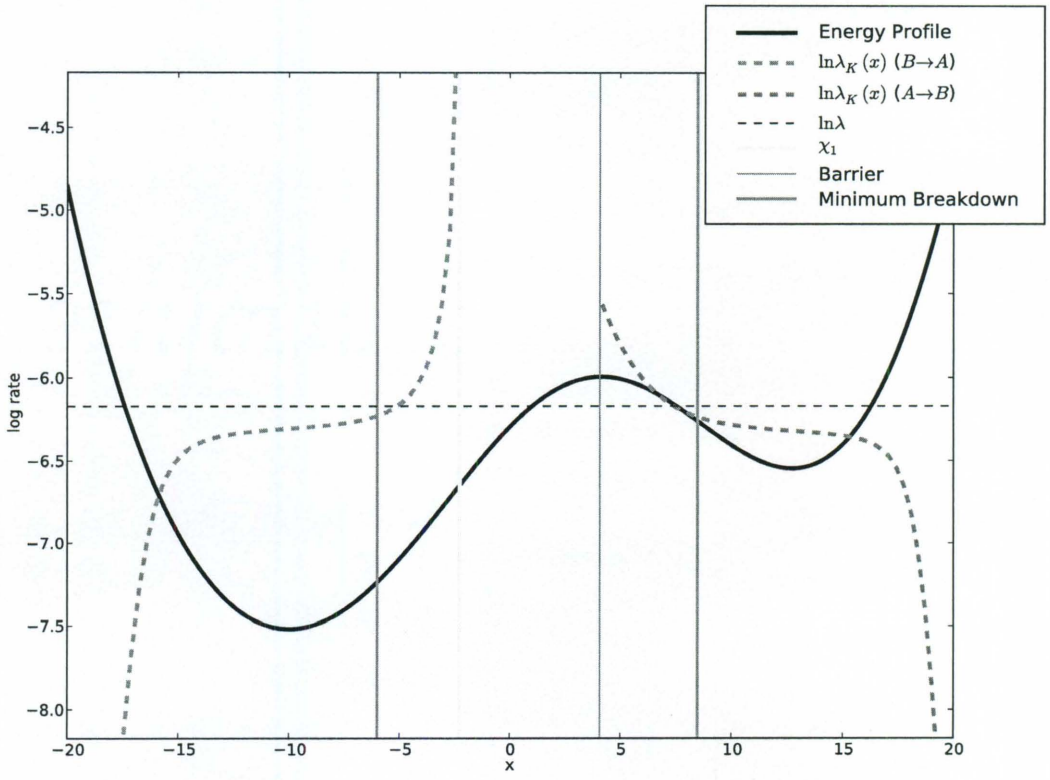

Figure 2.10 : The log of the reaction rates calculated by the escape Kramer's integral (Equation 1.28) for the depicted energy profile. The energy profile is provided for reference and is not to scale. The minimum mutual population and static current breakdowns, peak barrier and the χ_1 separatrix are indicated by vertical lines. The log of the reaction relaxation rate is indicated by a horizontal line.

System With Intermediate

In complicated reactions, there will be intermediate local minima between reactants and products. A simple example can be given by using a double internal barrier of the form

$$U_3(x) = k_3 \exp\left\{-a_3(x-\mu_3)^2\right\} + k_4 \exp\left\{-a_3(x-\mu_4)^2\right\} \tag{2.42}$$

with strengths $k_3 = 5.,\mathrm{kT}$, $k_4 = 5.,\mathrm{kT}$, width $a_3 = 5\mathrm{e}-2$, and centers at and $\mu_3 = 5.0$ and $\mu_4 = 4.0$. The composite system of the external barrier and symmetric internal barrier $V_3(x) = B(x) + U_3(x)$ is depicted in Figure 2.11.

In this example, we note a particular departure from the usual perspective taken in reaction rate approaches. Typical methods would prescribe application of Variational Transition State theory to the largest barrier along the reaction path at $\mu_3 = 5.0$, considering this an overestimate of the reaction rate due to recrossings caused by the local intermediate. In contrast, χ_1 separatrix theory shows the reaction rate can be calculated by considering either the barrier at μ_3 or μ_4 alone.

As in 2.2.1, the reaction rate can be calculated without crossing the largest barrier at μ_3. Figure 2.13 shows underestimate of the relaxation rate from the left due to inclusion of the population at the intermediate minima.

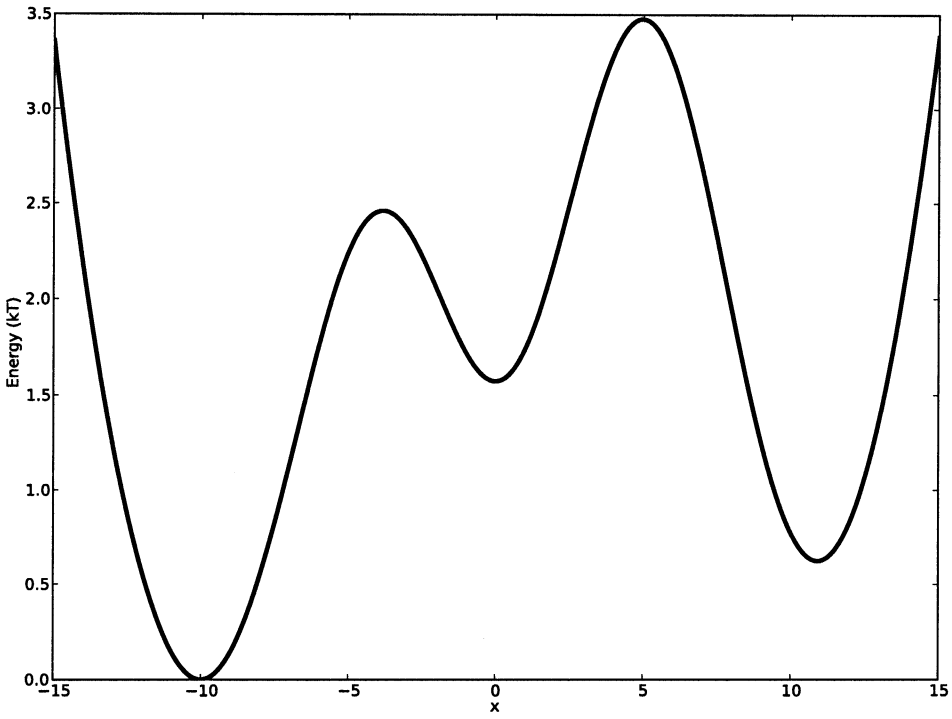

Figure 2.11 : The energy of the barrier potential with intermediate minima, $V_3(x) = B(x) + U_3(x)$, ($B(x)$ is given in Equation 2.39 and $U_3(x)$ in Equation 2.42)

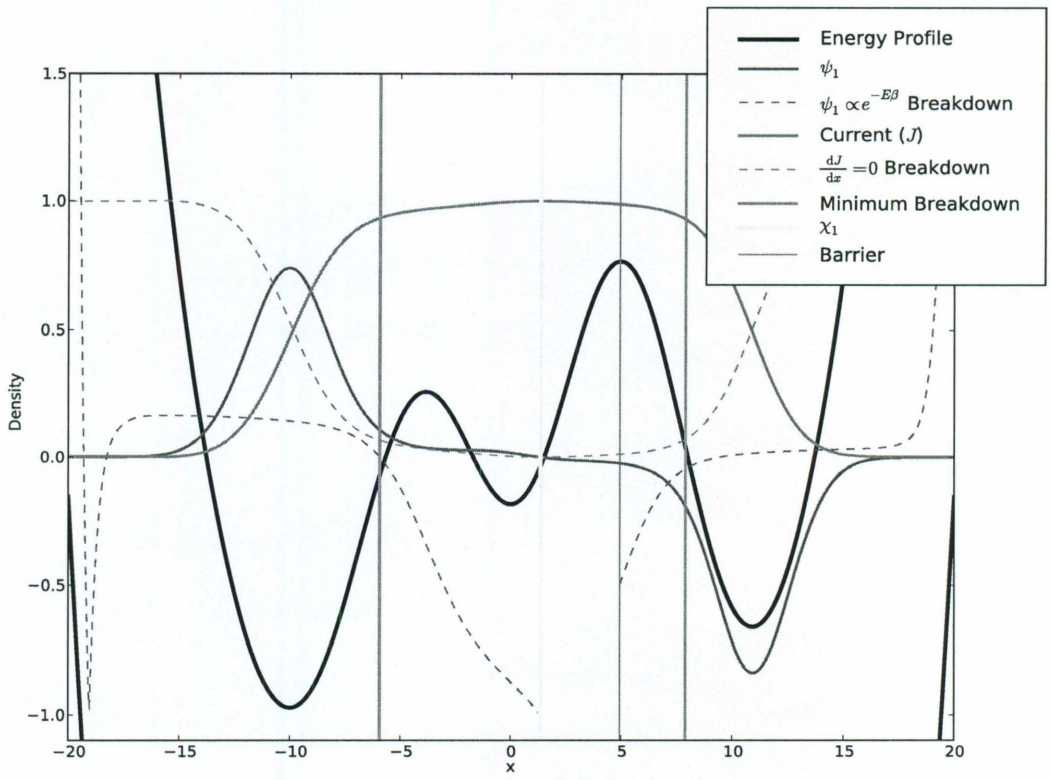

Figure 2.12 : The eigenfunction for the smallest non-vanishing eigenvalue, ψ_1, for the depicted energy profile; its associated current J, and the quantification of the breakdown in Kramer's assumptions as described in Section 2.2.1. The energy profile is provided for reference and is not to scale. The minimum mutual population and static current breakdowns, peak barrier and the χ_1 separatrix are indicated by vertical lines.

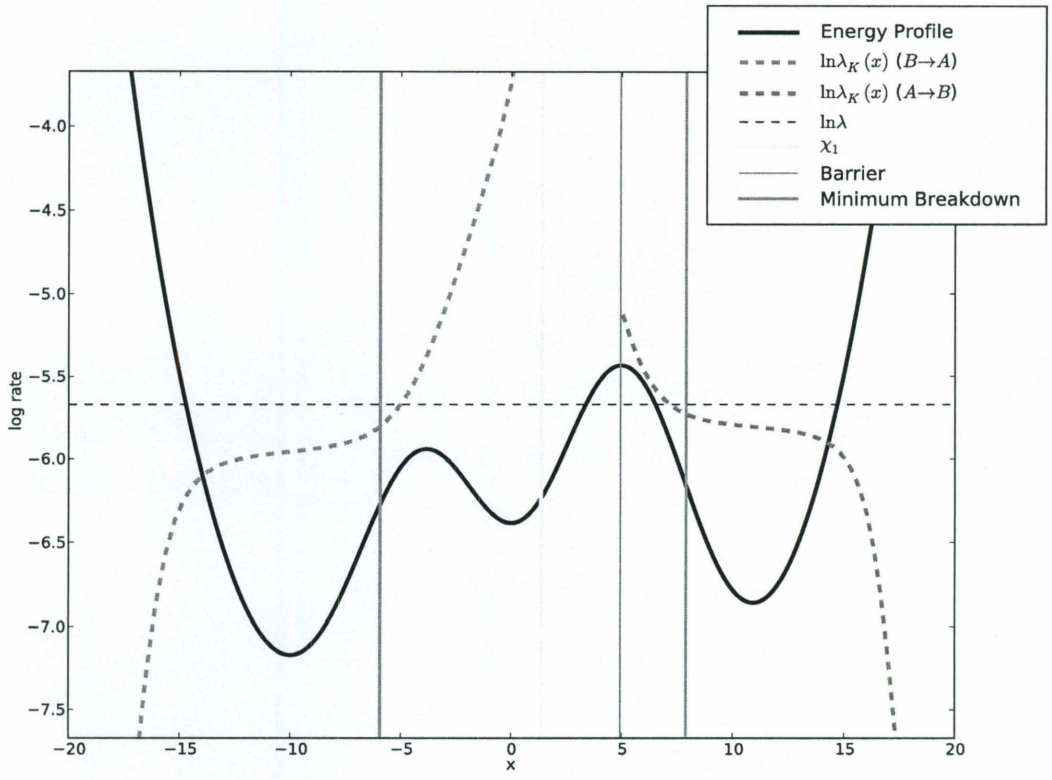

Figure 2.13 : The log of the reaction rates calculated by the escape Kramer's integral (Equation 1.28) for the depicted energy profile. The energy profile is provided for reference and is not to scale. The minimum mutual population and static current breakdowns, peak barrier and the χ_1 separatrix are indicated by vertical lines. The log of the reaction relaxation rate is indicated by a horizontal line.

Chapter 3

Super Symmetric Molecular Dynamics

Super symmetry is commonly known as a unifying theory in elementary particle physics. More generally, Super Symmetry refers to a formalism in which the mathematical objects under consideration, along with a pair of operators (the super symmetric charge operators), forms a Lie superalgebra. In physical systems, if the Hamiltonian of physical states is invariant under certain operations, then the system is said to have a symmetry defined by those operations. In the context of quantum mechanics, the physicality of super symmetric charge operators implies that for a given fermion quantum state, the charge operators applied to that state produce a bosonic state, different from all the fermionic states, with the same energy.

The similarity between the Fokker-Planck operator and the Schrodinger equation (as described in 1.2.3) suggest that it may be possible for a hidden super symmetry to exist for Fokker-Planck states. Indeed this is the case, and the super parters of the Fokker-Planck eigenfunctions are the associated currents: similarly to quantum super partners having the same energy, the population and its current decay at the same rate. By using the formalism of super symmetry, we are able to show the existence of a dynamical equation which is to the current as the Langevin equation (described in 1.2.1) is to the population density. This development was given by Kurchan and students for the Fokker-Planck equation[14, 15] and Kramer's equation[20]. We give an abridged discussion in Section 3.1.

The usefulness of such a dynamical equation becomes clear in the context of the Kramer's escape formulation described in Part2. Because the Kramer's escape rate formula depends on integrating over the regions near the χ_1 separatrix, where the

current flux is peaked (and hence nearly constant in space), accurate determination of contributing volumes is critical to determination of the rate constants*. In particular, we would like to integrate only over those configuration volumes which directly contribute to the escape time (a formula for doing this is given in Section 3.2).

However, besides being the regions of maximum current flux, because the critical regions are directly involved in the manifestation of a reaction time, they will also be amongst the rarest sampled trajectories for traditional Molecular Dynamics, which tends to *anneal* trajectories to the regions of large population density. What is sought is a method for annealing trajectories to regions of large current density. A dynamical Langevin equation for the super partners of the population density would do just this. The formalism of the super symmetry shows how to derive this equation.

In Section 3.1, we give the SuSy Kramer's equation, and show that an associated Langevin equation evolves the super partner density. The details of the evolution are explored in Section 3.1.4. In Section 3.1.4 we show that the previous prescription for using it fails to locate entropic wells. Then give a new prescription and demonstrations its use in simple models in Section 3.1.4. Finally, in section 3.2, we show how the populations derived from Super Symmetric Molecular dynamics can be used to compute escape times in a coordinate independent way.

3.1 The SuSy Kramer's and Langevin Equations

Until now, we have dealt almost exclusively with the analytically more amenable Fokker-Planck equation. In the context of Molecular Dynamics however, its more facile to treat systems realistically by retaining momentum. In this case we start out with the Kramer's equation (described in Section 1.2.1).

---

*Because Kramer's escape formula limits to classical Transition State Theory, these regions are important regardless of the transition state theory used.

3.1.1 The SuSy Kramer's Equation

Super symmetry in Kramer's equation is uncovered as in SuSy-QM by by "completing the square" of the diffusion operator. Once a pair of operators is found, it's enough to show they obey the right algebraic relations. The mathematical properties of these SuSy operators in the Fokker-Planck and Kramer's case are explored in detail by Kurchan and his students[14, 15, 20].

The underlying super symmetry in the Kramer's equation is revealed by "complicating" the operator with the introduction of $6N$ fermionic raising and lowering operators, $a_1, ..., a_{3N}, b_1, ..., b_{3N}$. Each of the a_i operators are associated with a spatial degree of freedom, and each of the b_i operators are associated with a momentum degree of freedom[†]. We abbreviate the complete set of spatial and momentum fermionic operators as $c_1, ..., c_{6N}$. By definition for fermionic operators, they satisfy the anti-commutation relations $\left[c_i,\ c_j^\dagger\right]_+ = \delta_{ij}$, and $\left[c_i,\ c_j\right]_+ = \left[c_i^\dagger,\ c_j^\dagger\right]_+ = 0$

The "number" of fermions associated with a state $|\psi\rangle$ can be determined by the fermion counting operator, $\hat{N} = \sum_j c_j^\dagger c_j$. The fermionic state with zero fermions is denoted $|-\rangle$, and defined by $c_i\,|c_i\rangle = |-\rangle$. We denote the occupied fermion states as $|c_i\rangle = c_i^\dagger|-\rangle$.

In the product space of phase space densities and fermionic states, $(|\mathbf{q}\rangle \otimes |\mathbf{p}\rangle \otimes |c_i\rangle)$, the SuSy Kramer's equation is

$$\frac{\partial}{\partial t}\,|\psi\rangle = \mathbf{H}_{\mathrm{SK}}\,|\psi\rangle = T(\mathbf{Q}\bar{\mathbf{Q}} + \bar{\mathbf{Q}}\mathbf{Q})\,|\psi\rangle\,, \tag{3.1}$$

where the SuSy "charge" operators are

$$\mathbf{Q} = -\mathrm{i}\sum_i \left[\frac{\partial}{\partial q_i}a_i + \frac{\partial}{\partial p_i}b_i\right] \tag{3.2}$$

$$\bar{\mathbf{Q}} = -\mathrm{i}\sum_i \left[b_i^\dagger\left(\frac{\partial}{\partial q_i} + \frac{1}{T}\frac{\partial \mathcal{H}}{\partial q_i}\right) - a_i^\dagger\left(\frac{\partial}{\partial p_i} + \frac{1}{T}\frac{\partial \mathcal{H}}{\partial p_i}\right) + \gamma b_i^\dagger\left(\frac{\partial}{\partial p_i} + \frac{1}{T}\frac{\partial \mathcal{H}}{\partial p_i}\right)\right], \tag{3.3}$$

[†]In the context of the SuSy Langevin equation (Section 3.1.2), the densities for these fermionic states are derived from the first moment of the distribution for a dynamical trajectory.

for the Hamiltonian $\mathcal{H}$. As an immediate consequence of the anticommunation properties of the fermion operators, we note that $\mathbf{Q}\mathbf{Q} = \bar{\mathbf{Q}}\bar{\mathbf{Q}} = \mathbf{0}$, and $\mathbf{Q}\psi|-\rangle = \mathbf{0}$.

Expanding the charge operator products and using the fermionic operator identities shows

$$\begin{aligned}\mathbf{H}_{\mathrm{SK}} &= T(\mathbf{Q}\bar{\mathbf{Q}} + \bar{\mathbf{Q}}\mathbf{Q}) \\ &= \mathbf{H}_{\mathrm{K}} + \sum_k \left(-a_k^\dagger b_k + \gamma b_k^\dagger b_k + \sum_l \frac{\partial^2 \mathcal{H}}{\partial q_k \partial q_l} b_k^\dagger a_l \right)\end{aligned} \tag{3.4}$$

The Kramer's operator eigenfunctions are the zero-fermion eigenfunctions of the SuSy Kramer's eigenfunctions, as can be seen by forming the product of a Kramer's eigenfunction, ψ_i, with the fermionic vaccum state:

$$\mathbf{H}_{\mathrm{SK}}\psi_i|-\rangle = T(\mathbf{Q}\bar{\mathbf{Q}} + \bar{\mathbf{Q}}\mathbf{Q})\psi_i|-\rangle = T\mathbf{Q}\bar{\mathbf{Q}}\psi_i|-\rangle = (\mathbf{H}_{\mathrm{K}}\psi_i)\,|-\rangle = \lambda_i\psi_i|-\rangle. \tag{3.5}$$

Then, the Kramer's operator eigenfunctions now have super partners with the same eigenvalue

$$\mathbf{H}_{\mathrm{SK}}\left(\bar{\mathbf{Q}}\psi_i|-\rangle\right) = T(\mathbf{Q}\bar{\mathbf{Q}} + \bar{\mathbf{Q}}\mathbf{Q})\bar{\mathbf{Q}}\psi_i|-\rangle = T\bar{\mathbf{Q}}\,\mathbf{Q}\bar{\mathbf{Q}}\psi_i|-\rangle = \lambda_i\bar{\mathbf{Q}}\psi_i|-\rangle. \tag{3.6}$$

The physical significance of the super partners can be seen by the fact that application of the raising charge operator, $\bar{\mathbf{Q}}$, to the eigenfunctions of the Kramer's equation, gives the "reduced current"[‡] in a form where each component of the current density vector is the density of the ith fermion:

$$\begin{aligned}\tilde{J}_{q_i} &= a_i\bar{\mathbf{Q}}\psi|-\rangle \\ \tilde{J}_{p_i} &= b_i\bar{\mathbf{Q}}\psi|-\rangle.\end{aligned} \tag{3.7}$$

[‡]The "reduced current" is distinct from the Kramer's current, but the difference is divergenceless, and so does not affect the evolution of population densities. The reduced current arises instead of the Kramer's current as a consequence of Kramer's operator not being Hermitizable. For our purposes we will not find reason to differentiate the reduced current and standard current.

Denoting the super partner states as a sum of one-fermionic states,

$$|\phi^{(1)}\rangle = \sum_{i=1}^{3N} \left(\tilde{J}_{q_i} a_i^\dagger + \tilde{J}_{p_i} b_i^\dagger \right) |-\rangle \tag{3.8}$$

$$= \sum_{i=1}^{3N} \begin{pmatrix} \tilde{J}_{q_i} \\ \tilde{J}_{p_i} \end{pmatrix} \begin{pmatrix} a_i^\dagger \\ b_i^\dagger \end{pmatrix} |-\rangle, \tag{3.9}$$

application of the SuSy Kramer's operator (Equation 3.4) shows the Kramer's super partners evolve according to

$$\begin{aligned}
\frac{\partial}{\partial t} |\phi^{(1)}\rangle &= \frac{\partial}{\partial t} \sum_{i=1}^{3N} \begin{pmatrix} \tilde{J}_{q_i} \\ \tilde{J}_{p_i} \end{pmatrix} \begin{pmatrix} a_i^\dagger \\ b_i^\dagger \end{pmatrix} |-\rangle \\
&= \mathbf{H}_{\mathrm{SK}} \sum_{i=1}^{3N} \begin{pmatrix} \tilde{J}_{q_i} \\ \tilde{J}_{p_i} \end{pmatrix} \begin{pmatrix} a_i^\dagger \\ b_i^\dagger \end{pmatrix} |-\rangle \\
&= \left[\mathbf{H}_{\mathrm{K}} + \sum_k \left(-a_k^\dagger b_k + \gamma b_k^\dagger b_k + \sum_l \frac{\partial^2 \mathcal{H}}{\partial q_k \partial q_l} b_k^\dagger a_l \right) \right] \sum_{i=1}^{3N} \begin{pmatrix} \tilde{J}_{q_i} \\ \tilde{J}_{p_i} \end{pmatrix} \begin{pmatrix} a_i^\dagger \\ b_i^\dagger \end{pmatrix} |-\rangle \\
&= \sum_{i=1}^{3N} \left[\mathbf{H}_{\mathrm{K}} + \sum_j \begin{pmatrix} 0 & -\delta_{ij} \\ \frac{\partial^2 \mathcal{H}}{\partial q_i \partial q_j} & \gamma \delta_{ij} \end{pmatrix} \right] \begin{pmatrix} \tilde{J}_{q_j} \\ \tilde{J}_{p_j} \end{pmatrix} \begin{pmatrix} a_i^\dagger \\ b_i^\dagger \end{pmatrix} |-\rangle
\end{aligned} \tag{3.10}$$

The utility of the SuSy formulation is seen here by the simplicity of the derivation of the diffusion equation for the current. Similarly to the manner in which manipulation of complex trigonmetric funtions is made easier by extending the function into the complex field and using Euler's equation, the dynamical equation for diffusion currents is more easily derived by extending the function space with fermionic operators and using the SuSy Kramer's operator.

3.1.2 SuSy Langevin Dynamics

Conceptually, the most surprising aspect of the SuSy Langevin dynamics is seen in the contrast to the relation between Langevin dynamics and Kramer's population. Whereas the population density of the Kramer's equation is *directly* evolved by the

Langevin equation, the population density of the SuSy Kramer's equation is the first moment of the "compass vector" population evolved by the SuSy Langevin equation.

The SuSy Langevin equation is formed by extending the standard Langevin dynamics for a given system (Equation 1.6) by associating to each trajectory $(\mathbf{q}(t), \mathbf{p}(t))$ a $3N$ dimensional oscillator, $(\mathbf{u}(t), \mathbf{w}(t))$, which evolves according to the non-stochastic dissipative equation

$$\begin{aligned} \frac{\partial u_i}{\partial t} &= w_i \\ \frac{\partial w_i}{\partial t} &= -\gamma w_i + \sum_j \frac{\partial^2 \mathcal{H}}{\partial q_i \partial q_j}(\mathbf{q}) u_j. \end{aligned} \tag{3.11}$$

These can be seen as the dynamical equation with friction (similar to Equation 1.6 without stochastic impulses) for the Harmonic Oscillator Hamiltonian

$$\mathcal{H}' = \frac{1}{2}\mathbf{w}^2 + \mathbf{u}^T \mathbf{H}(\mathbf{q}) \mathbf{u} \tag{3.12}$$

where $\mathbf{H}$ is the Hessian of the potential energy in $\mathcal{H}$. Equation 3.11 is different form from the original prescription for the SuSy Langevin[20, 17], but remains equivalent and is physically more intuitive. It is also easier to recognize an effective means to integrate the extended system: we integrate the composite trajectory and compass vector using Manella's quasisymplectic integrator[16] with a generalized thermostat which is zero for the compass component.

We write the population of trajectories at $(\mathbf{q}, \mathbf{p})$ with compass vector $(\mathbf{u}, \mathbf{w})$ as $F(\mathbf{q}, \mathbf{p}, \mathbf{u}, \mathbf{w})$. Because the underlying Langevin dynamics is not modified, the components of the current for F in the $(\mathbf{q}, \mathbf{p})$ phase space (Equation 1.9) are not modified, and the current in the $(\mathbf{u}, \mathbf{w})$ phase space are the non-stochastic population currents

$$\mathbf{J}_{u_i} = w_i F \tag{3.13}$$

$$\mathbf{J}_{w_i} = \left(\gamma w_i + \sum_j \frac{\partial^2 H}{\partial q_i \partial q_j}(\mathbf{q}) u_j \right) F, \tag{3.14}$$

The continuity equation for the four currents of F is

$$\frac{\partial F}{\partial t} = -\left(\mathbf{H}_\mathrm{K} + \sum_i \frac{\partial}{\partial u_i} w_i + \frac{\partial}{\partial w_i} \left(\gamma w_i + \frac{\partial^2 H}{\partial q_i \partial q_j}(\mathbf{q}) u_i \right) \right) F. \tag{3.15}$$

Then, the first moment of the compass vector phase space for F at each $\mathbf{q}$ and $\mathbf{p}$ evolves as

$$\frac{\partial}{\partial t}\int \begin{pmatrix} u_i \\ w_i \end{pmatrix} F(\mathbf{q},\mathbf{p},\mathbf{u},\mathbf{w})\,\mathrm{d}\mathbf{u}\,\mathrm{d}\mathbf{w} \tag{3.16}$$

$$= \int \begin{pmatrix} u_i \\ w_i \end{pmatrix} \left(-\mathbf{H}_\mathrm{K} - \sum_j \frac{\partial}{\partial u_j} w_j \right. \tag{3.17}$$

$$\left. + \frac{\partial}{\partial w_j}\left(\gamma w_j + \frac{\partial^2 H}{\partial q_j \partial q_j}(\mathbf{q}) u_j\right) F(\mathbf{q},\mathbf{p},\mathbf{u},\mathbf{w}) \right) \mathrm{d}\mathbf{u}\,\mathrm{d}\mathbf{w} \tag{3.18}$$

$$= -\mathbf{H}_\mathrm{K} \int \begin{pmatrix} u_i \\ w_i \end{pmatrix} F\,\mathrm{d}\mathbf{u}\,\mathrm{d}\mathbf{w} \tag{3.19}$$

$$+ \sum_j \int \begin{pmatrix} u_i \frac{\partial}{\partial u_j} w_j + \frac{\partial}{\partial w_j}\left(\gamma w_j + \frac{\partial^2 H}{\partial q_j \partial q_j}(\mathbf{q}) u_j\right) F \\ w_i \frac{\partial}{\partial u_j} w_j + \frac{\partial}{\partial w_j}\left(\gamma w_j + \frac{\partial^2 H}{\partial q_j \partial q_j}(\mathbf{q}) u_j\right) F \end{pmatrix} \mathrm{d}\mathbf{u}\,\mathrm{d}\mathbf{w} \tag{3.20}$$

The distribution of F is L_1 in u and w because the the continuity equation guarantees preservation of the total population. Then application of Gauss' theorem gives

$$= -\mathbf{H}_\mathrm{K} \int \begin{pmatrix} u_i \\ w_i \end{pmatrix} F\,\mathrm{d}\mathbf{u}\,\mathrm{d}\mathbf{w} + \sum_j \int \begin{pmatrix} u_i \frac{\partial}{\partial u_j} w_j F \\ w_i \frac{\partial}{\partial w_j}\left(\gamma w_j + \frac{\partial^2 H}{\partial q_j \partial q_j}(\mathbf{q}) u_j\right) F \end{pmatrix} \mathrm{d}\mathbf{u}\,\mathrm{d}\mathbf{w}, \tag{3.21}$$

Finally, integration by parts shows

$$= -\mathbf{H}_\mathrm{K} \int \begin{pmatrix} u_i \\ w_i \end{pmatrix} F\,\mathrm{d}\mathbf{u}\,\mathrm{d}\mathbf{w} + \sum_j \int \begin{pmatrix} -w_j F \\ \left(\gamma w_j + \frac{\partial^2 H}{\partial q_j \partial q_j}(\mathbf{q}) u_j\right) F \end{pmatrix} \mathrm{d}\mathbf{u}\,\mathrm{d}\mathbf{w} \tag{3.22}$$

$$= \left(-\mathbf{H}_\mathrm{K} + \sum_j \begin{pmatrix} 0 & -\delta_{ij} \\ \frac{\partial^2 H}{\partial q_j \partial q_j}(\mathbf{q}) & \gamma \end{pmatrix} \right) \int \begin{pmatrix} u_i \\ w_i \end{pmatrix} F\,\mathrm{d}\mathbf{u}\,\mathrm{d}\mathbf{w} \tag{3.23}$$

which is the same as the evolution we expect for the components of the fermion densities in Equation 3.10 when we identify

$$\begin{pmatrix} \mathbf{J}_{q_i} \\ \mathbf{J}_{p_i} \end{pmatrix} = \int \begin{pmatrix} u_i \\ w_i \end{pmatrix} F\,\mathrm{d}\mathbf{u}\,\mathrm{d}\mathbf{w}. \tag{3.24}$$

This elucidates the meaning of the term "compass vector," because the vectors point on average in the direction the population distribution will move.

3.1.3 Cloning and Destroying

In Section 2.1.2, we showed that the flux of the current distribution peaks on the χ_1 separatrix plane dividing the reactant and product states. From Equation 3.24 we expect the first moment of the compass vectors to be the largest, and rapidly anneal to the large moment on on a short time scale in these same regions. However, it should be difficult to accurately calculate the average in Equation 3.24 if it depends on a population of compass vectors carried by rare trajectories moving between metastable states. The difficulty of accurate computation of this average is overcome by increasing the population in regions of large compass vector magnitude.

We note that the first moment in Equation 3.24 would be the same if population of compass vectors at $F(q,p,u,w)$ (from Section 3.1.2) were replaced by a population $\sqrt{u^2+w^2}F(q,p,u,w)$ with vectors of unit magnitude. Writing the compass vector as $(\mathbf{u},\mathbf{w}) = |(\mathbf{u},\mathbf{w})|\,\widehat{(\mathbf{u},\mathbf{w})}$, we see the first moment is still the same

$$(\mathbf{J}_{q_i},\mathbf{J}_{p_i}) = \int (\mathbf{u},\mathbf{w}) F \,\mathrm{d}\mathbf{u}\,\mathrm{d}\mathbf{w} \tag{3.25}$$

$$= \int \widehat{(\mathbf{u},\mathbf{w})}\,|(\mathbf{u},\mathbf{w})|\,F \,\mathrm{d}\mathbf{u}\,\mathrm{d}\mathbf{w}. \tag{3.26}$$

Although it was not the originally stated intention, this effect can be accomplished by incorporating of cloning and destroying of trajectories depending on the compass vectors. The effect is to replace compass vectors with large magnitudes with a commensurate large number of independent trajectories. By doing this, instead of keeping all the information about the first fermionic population in a few rare and undersampled trajectories, we use the size of the compass to indicate regions where additional sampling is worthwhile to give accurate characterization of the regions with large current.

The effect on trajectories of cloning is depicted in Figure 3.1. When cloning

is performed, we create an identical trajectory at the same point in the extended phase space, which then evolves independently according to its own unique sequence of stochastic perturbations $\eta(t)$ in Equation 1.6. After destroying a trajectory, the trajectory is removed from further simulation. The rate at which the population changes is

$$\mathcal{R}(u,w) = \frac{\frac{\partial}{\partial t}\sqrt{\mathbf{w}^2+\mathbf{u}^2}}{\sqrt{\mathbf{w}^2+\mathbf{u}^2}} \tag{3.27}$$

where the time dependence of $\mathbf{w}$ and $\mathbf{u}$ is given by Equation 3.11. To change the population at this rate, we give each trajectory a probability $N(u,w)\,\mathrm{d}t$ of being cloned when $N(u,w) > 0$, and a probability $|N(u,w)|\,\mathrm{d}t$ of being destroyed when $N(u,w) < 0$.

With the rate $\mathcal{R}$, if the all the clones experienced nearly identical stochastic forces and followed the same trajectory, the total number of clones would be, averaging over repeated simulations, equal to the absolute change in the magnitude of the compass vector without cloning. To see this, we consider a trajectory where the norm of compass vector changes from $W_1 = \sqrt{[\mathbf{w}(t_1)]^2+[\mathbf{u}(t_1])^2} = 1$ to $W_2 = \sqrt{[\mathbf{w}(t_2)]^2+[\mathbf{u}(t_2])^2}$ in the time interval t_1 to t_2; and write the total number of clones in the ensemble at time t as $N(t)$ with $N(t_1) = 1$. The change of the population in time satisfies $\frac{\partial}{\partial t}N = \mathcal{R}(t)N$. Integration immediately shows $\ln(N_2) = \int_{t_1}^{t_2}\mathcal{R}(t)\,\mathrm{d}t = \ln(W_2)$.

Because the number of clone partners would conserve the total vector norm and direction if the trajectory was nearly deterministic, we can compute the moment in Equation 3.25 by integrating the *normalized* compass vectors of the full population including clones. In general, the SuSy Langevin trajectories would follow different paths and thus form a more complete picture of the compass vector ensemble for computation of the average in Equation 3.25.

In Section 3.1.4, because of the problems described in Section 3.1.4, we further modify this technique to normalize the trajectory current density back to a Kramer's density.

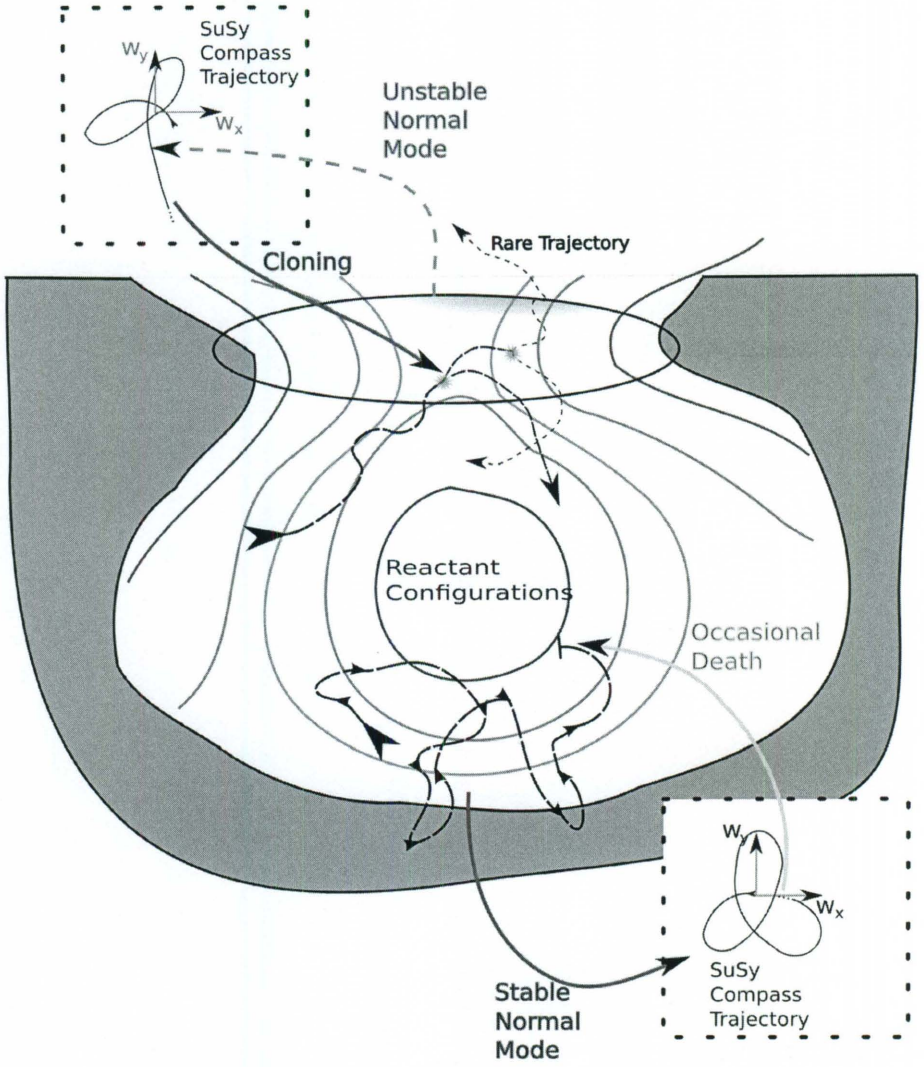

Figure 3.1 : The compass vector vectors accompanying the molecular dynamics trajectories described in Section 3.1.2 diverge from the origin in their coordinate system when the trajectory carrying them traverses energetic saddle points. When the trajectories are cloned at the rate described in Equation 3.27, sampling of rare trajectories involved metastable transitions is increased.

3.1.4 Analysis of Compass Behavior

We can gain an intuitive understanding of the regions in configuration space where the cloning described in Section 3.1.3 occurs by analyzing the instantaneous behavior of the compass vectors in terms of the dynamics described by Equation 3.11.

The compass vector dynamics depend only indirectly on the system phase space (q, p) through the Hessian $\mathbf{H}(q(t))$. Because the compass vectors do not affect the motion of the trajectory that carries them, to the perspective of the compass vectors the motion is simply that of an $3N$ dimensional oscillator with time dependent stochastic frequency $\mathbf{H}(q(t))$. If we assume the energy is a smooth function of q, $\mathbf{H}(q(t))$ will be approximately constant for short periods of time as the underlying trajectory traverses the potential; and we may approximate the instantaneous motion of the compass vectors with a constant Hessian $\mathbf{H} \equiv \mathbf{H}(\mathbf{q})$. This approximation will become exact for long periods in the special cases where $\mathbf{H}(\mathbf{q})$ is constant in a large region of configuration space (as occurs for instance in the Entropic well in Figure 1.2 and in barrier deflection in sections 3.1.4 and 3.1.4).

Then, the form of the rate in Equation 3.27 shows that the instantaneous changes in the population due to cloning and destroying can be immediately seen from the instantaneous change in the compass vector magnitude.

To simplify matters, we block diagonalize $\mathbf{H}$ in terms of the orthogonal matrix of normal modes $\mathbf{Q}$ and diagonal matrix of force constants $\mathbf{L}$ so that $\mathbf{H} = \mathbf{Q}\mathbf{L}\mathbf{Q}^T$. For the instantaneous intervals of time where the approximation of $\mathbf{H}$ being constant is valid, the vibrational modes evolve independently of one another and we can analyze them separately. For the actual time dependent motion the vectors describing the normal modes will gradually change with the motion of the trajectory as the trajectory commutes between local minima and tend to mix the motion of the modes over time. It is this mixing which allows the compass vectors to (statistically) learn the topology of the energy surface and anneal the population to reaction currents.

We can decompose the compass vector components in terms of the local vibrational

modes of $\mathbf{Q}$ in the local coordinates $\mathbf{a}$ and $\mathbf{b}$ as

$$\mathbf{u} = \mathbf{Q}\mathbf{a} = \sum_i \mathbf{Q}\mathbf{e}_i a_i \tag{3.28}$$

$$\text{and } \mathbf{w} = \mathbf{Q}\mathbf{b} = \sum_i \mathbf{Q}\mathbf{e}_i b_i \tag{3.29}$$

We see the evolution in terms of the local coordinates by applying Equation 3.11,

$$\begin{pmatrix} \dot{\mathbf{u}} \\ \dot{\mathbf{w}} \end{pmatrix} = \sum_i \mathbf{Q}\mathbf{e}_i \begin{pmatrix} \dot{a}_i \\ \dot{b}_i \end{pmatrix} = - \begin{pmatrix} 0 & -\mathbf{I} \\ \mathbf{H} & \gamma\mathbf{I} \end{pmatrix} \left(\sum_i \mathbf{Q}\mathbf{e}_i \begin{pmatrix} a_i \\ b_i \end{pmatrix} \right) \tag{3.30}$$

$$= - \sum_i \begin{pmatrix} 0 & -\mathbf{Q}\mathbf{e}_i \\ \mathbf{H}\mathbf{Q}\mathbf{e}_i & \gamma\mathbf{Q}\mathbf{e}_i \end{pmatrix} \begin{pmatrix} a_i \\ b_i \end{pmatrix} \tag{3.31}$$

$$= - \sum_i \mathbf{Q}\mathbf{e}_i \begin{pmatrix} 0 & -1 \\ \Lambda_i & \gamma \end{pmatrix} \begin{pmatrix} a_i \\ b_i \end{pmatrix}. \tag{3.32}$$

Where Λ_i is the force constant for vibration for the mode $\mathbf{Q}\mathbf{e}_i$. The linear independence of the modes $\mathbf{Q}\mathbf{e}_i$ in Equation 3.30 indicates we can give the equations of motion for each mode independently by

$$\begin{pmatrix} \dot{a}_i \\ \dot{b}_i \end{pmatrix} = \begin{pmatrix} 0 & -1 \\ \Lambda_i & \gamma \end{pmatrix} \begin{pmatrix} a_i \\ b_i \end{pmatrix}. \tag{3.33}$$

The solution to this linear system is well known to be

$$\begin{pmatrix} a_i \\ b_i \end{pmatrix} = -\exp \left\{ \begin{pmatrix} 0 & -1 \\ \Lambda_i & \gamma \end{pmatrix} t \right\} \begin{pmatrix} a_{i,0} \\ b_{i,0} \end{pmatrix}. \tag{3.34}$$

This form can be simplified further in terms of the eigen properties of propagating matrix

$$\begin{pmatrix} 0 & -1 \\ \Lambda_i & \gamma \end{pmatrix}. \tag{3.35}$$

The eigenvalues of the propragating matrix are

$$\lambda_\pm = \frac{\gamma \pm \sqrt{\gamma^2 - 4\Lambda_i}}{2} \tag{3.36}$$

The spectrum is depicted in Figure 3.2. Taking the associated eigenvectors of λ_+ and λ_- as $\mathbf{q}_+$ and $\mathbf{q}_-$ respectively, and writing the intitial condition as

$$\begin{pmatrix} a_{i,0} \\ b_{i,0} \end{pmatrix} = c_-\mathbf{q}_- + c_+\mathbf{q}_+ \tag{3.37}$$

the time dependent solution in Equation 3.34 can be written

$$\begin{pmatrix} a_i \\ b_i \end{pmatrix} = c_-\exp\{-\lambda_- t\}\,\mathbf{v}_- + c_+\exp\{-\lambda_+ t\}\,\mathbf{v}_+. \tag{3.38}$$

The implication is that the compass vector component along in the linear space of the given mode will tend towards position and velocity components in the direction of the eigenvector with eigenvalue having smallest real part. If both eigenvalues are positive, it will eventually decay toward the origin, corresponding to termination of the trajectory.

For a given friction constant γ, the eigenvalues for the motion of the ith vibrational mode depend on the frequency of vibration for the undamped oscillator mode Λ_i as depicted in Figure 3.36. We can see from Figure 3.36 four primary regions with characteristic behavior: In the underdamped region where there the force constant of curvature is $\Lambda_i > \gamma^2/4$, the motion of the compass vector will oscillate with frequency $\mathrm{Im}\{\lambda_+\}$ and decaying amplitude $\mathrm{Re}\{\lambda_+\} = \gamma/2$. In the region where $0 < \Lambda_i < \gamma^2/4$, the compass vector amplitude decays very slowly to 0. In the special case of $\Lambda_i = 0$, the compass vector approaches a stationary state, not necessarily 0, dependent on its initial condition at the rate γ. Finally, in the unstable region where $\Lambda_i < 0$, the eigenvalues $\lambda_\pm$ are completely real, and the compass trajectory magnitude exponentially *increases* in the direction of the eigenvector with eigenvalue λ_-.

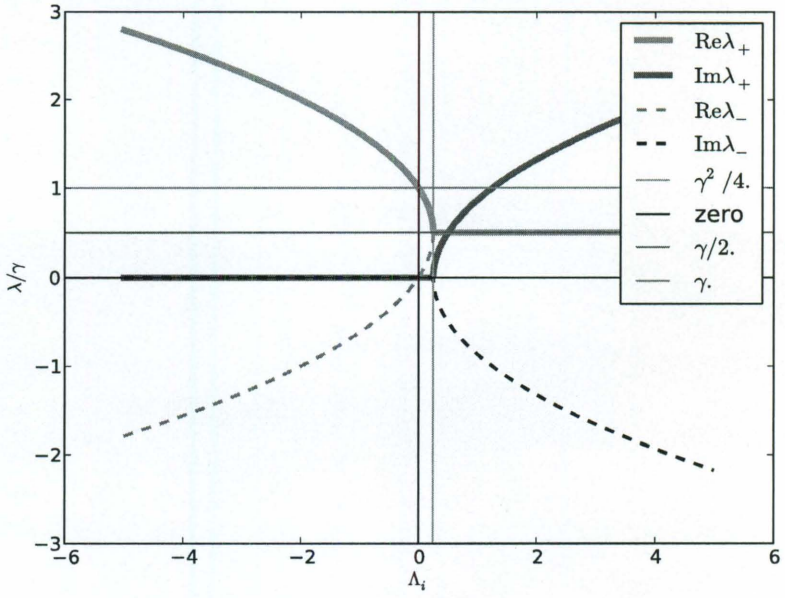

Figure 3.2 : Spectrum of eigenvalues for the motion of compass vectors in Equation 3.38 with a given friction constant γ.

Barrier Deflection

An important case to consider the motion of the compass vectors determined by Equation 3.11 is the case where the trajectory carrying the compass vector is reflected by a perfectly elastic wall. It is intuitively clear that the effect of the impact on the trajectory is to reflect the velocity component normal to the surface. It turns out that the effect of the impact on the compass vector is to reflect the components of both $\mathbf{u}$ and $\mathbf{w}$ normal to the surface.

To demonstrate this, we consider a one-dimensional potential which becomes the Heaviside function in the limit $a \to 0$:

$$V(x) = \begin{cases} 0 & x < -a \\ \frac{V_0}{a^2}(x+a)^2 & -a \leq x \text{ and } x \leq 0 \\ V_0 & x > 0 \end{cases} \cdot \tag{3.39}$$

We assume a particle governed by the Langevin dynamics (Equation 1.6) is incident incident on the harmonic potential from the negative x region with velocity in the positive direction, with insufficient energy to overcome the barrier. The incident particle would then experience a harmonic force tending to return it to the free particle region with a negative velocity. In the limit $a \to 0$, the force constant of the harmonic potential becomes so great that the effects of friction and the stochastic forces η can be neglected. Then, trajectory will undergo a half-period of oscillation, the symmetry of which returns the trajectory to the negative x region with reflected velocity.

While in the harmonic potential, the force experienced by the compass vector will be that of a symmetric harmonic potential with the same force constant. As a consequence, in the limit $a \to 0$, the compass trajectory experiences oscillatory motion with the same frequency as the carrying trajectory for a half-period of oscillation. The symmetry of the motion gives a reflected $\mathbf{u}$ and $\mathbf{w}$ upon the carrying trajectory's return to the negative x region.

Entropic Well

Previous techniques developed to explore energetic landscapes have focused on locating potential energy barriers, as opposed to free energy barriers[21, 10]. Whereas we summarised Section 1.1.2 that in complex reactions, identification of free energy barriers tend to be more important, and more challenging. Super Symmetric Molecular Dynamics(SuSyMD) has been proposed as a means of identifying free energy barriers. In this section, we explain why the previously described methods [15, 20, 17] are unable to identify entropic only free energy barriers, and in Section 3.1.4 describe a way to modify SuSyMD so that it will.

Free energy, as a combination of both energy and entropy, can be characterized in two extremes: entropic barriers and energetic barriers. Energetic barriers are characterized by regions of negative curvature: if a region of high energy separates two local energetic minima, the potential energy must be decreasing from the top of the barrier towards either of the minima. In Section 3.1.4, we saw that negative curvature causes SuSy the component of compass vectors to exponentially increase in magnitude parallel to unstable normal mode, while the stable components in the orthogonal directions would decay. It follows that locating regions where the compass vectors tend to all be aligned in one direction would evince energetic saddle points. So while the ability to identify energetically dominated free energy barriers is clear, in previous work [17, 15], it was suggested that these correlations would also indicate entropic barriers.

However, because the previous methods rely solely on analysis of the compass vectors, they will not be able to detect entropically dominated free energy barriers without carefully chosen initial conditions. To show this, we consider "entropic well" systems, characterized by perfectly elastic walls surrounding flat energy regions, as depicted in Figure 1.2.

In entropic well systems, the compass vectors have two modes of behavior for the reasons described in Section 3.1.4. In the regions of constant energy, the compass

vectors behave like free particles with friction and rapidly move to a time independent state on a timescale of the inverse friction, independent of the carrying trajectory. When the particles collide with the walls, the components of the compass vectors normal to the wall are reflected, changing direction but not magnitude for the reasons described in Section 3.1.4.

Now, we suppose that a population SuSyMD of trajectories is incident on the entropic barrier with randomized compass vectors (i.e., the trajectories have initially have no knowledge of the barrier). A cartoon of the situation where SuSyMD trajectories are incident on the barrier is depicted in figures 3.3 and 3.4. After the collision with the barrier, the compass vectors of the trajectories which pass through the opening will not change, while the compass vectors of the trajectories which were reflected will be reflected. Although some of the compass vectors are reflected, because the ensemble of compass vectors was random before the collision, the ensemble of compass vectors will still be random after the collision and analysis of the compass vectors alone will not yield information about the barrier. This is in marked contrast to an ensemble of compass vectors incident on an energetic saddle point (depicted in figures 3.5 and 3.6), where the unstable negative curvature causes rapid differentiation between the compass vectors which traverse the saddle point and those which are reflected.

It is important to note that this argument does *not* imply that the SuSy Langevin equation fails to anneal to a reactant current in this case. The failure of SuSy Langevin dynamics here represents an extreme sensitiviy to initial conditions in the purely entropic case. If the compass vectors incident on the entropic barrier had been aligned with the entropic passage before the collision, the compass vectors of the ensemble which were reflected would have had their components normal to the wall randomized from the stochastic collisions with the wall; meanwhile, the transmitted ensemble would have have their orthogonal components randomized. The resulting populations would have correlation along the direction of current.

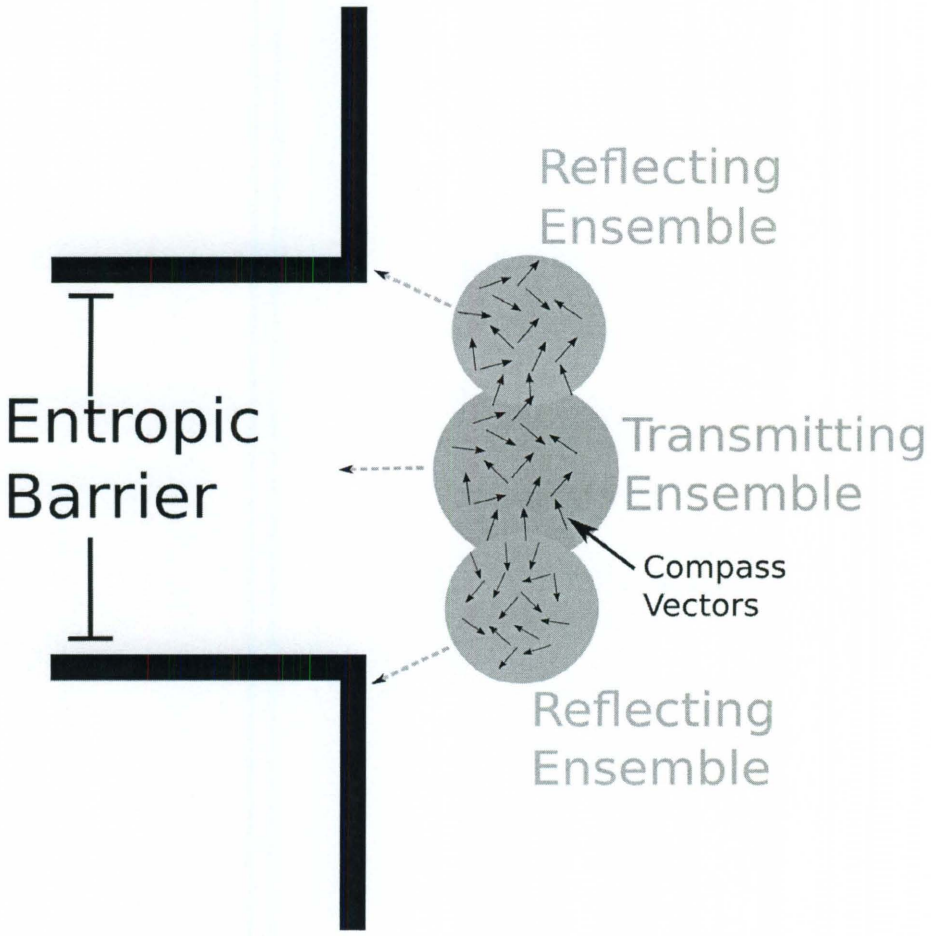

Figure 3.3 : This cartoon depicts an ensemble of trajectories with initially randomized walker vectors incident on an entropic barrier before the collision. The subensembles which will eventually reflect from the walls and the subensemble which will transmit are indicated.

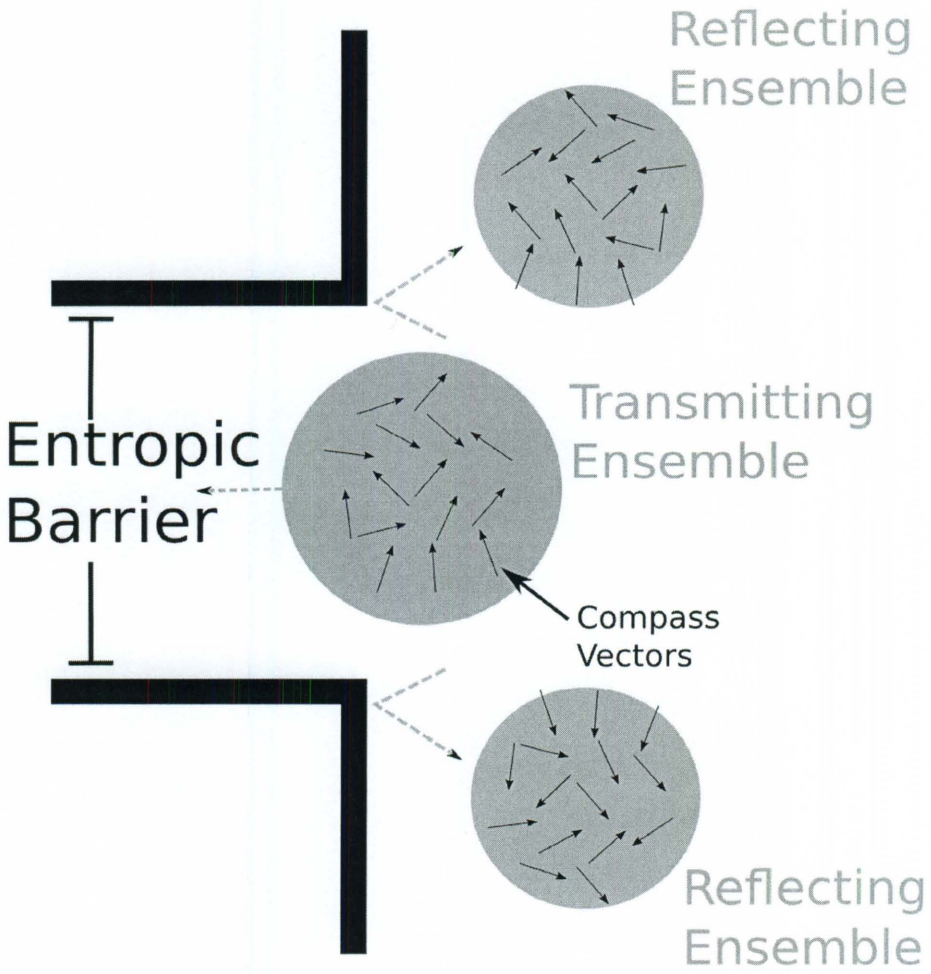

Figure 3.4 : This cartoon depicts an ensemble of trajectories with initially randomized walker vectors incident on an entropic barrier after the collision expected in Figure 3.3. The subensembles which were reflected from the walls and the subensemble which were transmitted are indicated. The compass vectors associated with the reflected trajectories have been reflected but are still randomized. There is no distinguishing property within the compass vector ensemble which indicates the presence of the barrier.

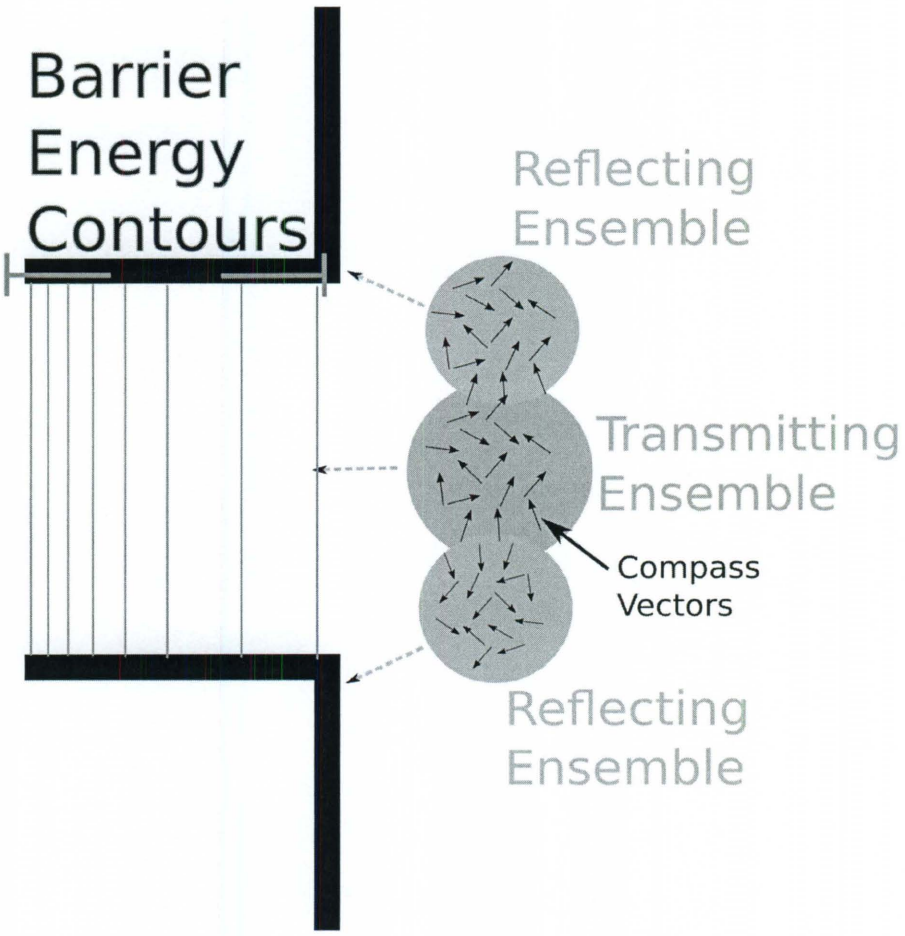

Figure 3.5 : This cartoon depicts an ensemble of trajectories (identical to those in Figure 3.3) with initially randomized walker vectors incident on an narrow *energetic* barrier before the collision. The subensembles which will eventually reflect from the walls and the subensemble which will transmit are indicated.

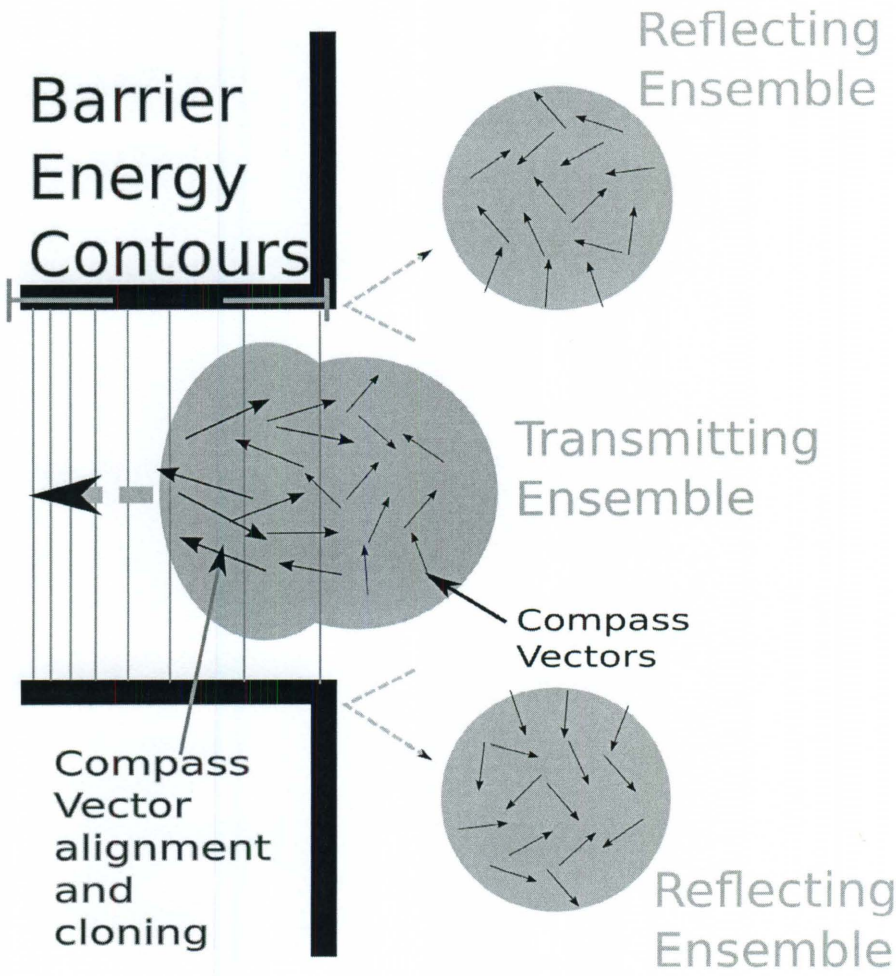

Figure 3.6 : This cartoon depicts an ensemble of trajectories with initially randomized walker vectors incident on a narrow *energetic* barrier after the collision expected in Figure 3.5. The subensembles which were reflected from the walls and the subensemble which were transmitted are indicated. In contrast to the entropic barrier case in Figure 3.4, the compass vectors in the transmitted subensemble rapidly change in the presence of the negative energetic curvature of the barrier, and can be distinguished by analysis of the compass vectors

In general, we would like a method could locate entropic barriers without foreknowledge of the current direction. To mend this problem, we change the prescribed method for using SuSyMD to one in which analysis is performed on the carrying trajectories rather than on the compass vectors alone. This method is able to detect both energetic and entropic barriers as demonstrated in Section 3.1.5.

SuSy MD as an ensemble magnifying glass

As we showed in Section 3.1.4, methods for the detection of free energy barriers which focus solely on SuSy compass vectors are unable to identify entropic barriers. This fact is surprising when we consider (in Section [add ref entropic well]) that Molecular Dynamics (MD) is, by itself, able to identify entropic barriers. What we would like is a method that combines the ability of MD to identify entropic barriers with SuSy MD's ability to enhance sampling of rare trajectories over energetic barriers.

In Section 3.1.4, we show that direct analysis of the MD trajectories carrying the SuSy compass vectors will not represent a physically correct Kramer's population distribution due to the perturbation of the population by cloning and destroying. In order to reclaim a realistic Fokker-Planck density, we reweight the MD trajectories according to the principles of Ensemble Magnifying technique described in Section 3.1.4. This yields a physically correct population density, while retaining the enhanced sampling density on energetic barriers, giving a detailed picture of the desired probability current.

Ensemble Magnifying Glass

The primary impediment in the simulation of rare events in chemical systems is the requirement for the transition probabilities in the simulation to have the property of detailed balance (defined below). Rare events in chemical simulations by definition are associated with states that have small population densities at equilibrium. This property necessarily makes them difficult to explore without violating detailed balance. In this section, we discuss a method for enhancing the simulation of rare events without violating detailed balance which dovetails with the cloning behavior in SuSyMD.

We consider a time dependent population, $P(x,t)$ of possible states x at time t, which comprises of a large number of Molecular Dynamics trajectories. To obtain a population density, we simulate a large ensemble of N trajectories, each having a

time dependent state $x_k(t)$. The time dependent population density is then

$$P(x,t) \approx \sum_k \delta(x_k(t) - x), \tag{3.40}$$

where $\delta(x_k - x)$ is a function which is non-zero only when $x_k \approx x$, and $\int \delta(x)\,\mathrm{d}x = 1$.

Whatever method is used to integrate the trajectories, the method should satisfy the condition of detailed balance. The condition for detailed balance is that the probability, $T(x_i, x_j; t_1, t_2)$, for a configuration in state x_i at time t_1 to be found in state x_j at a later time t_2 is related to the equilibrium population $P_0(x_i)$ by

$$T(x_i, x_j; t_1, t_2)P_0(x_i) = T(x_j, x_i; t_1, t_2)P_0(x_j). \tag{3.41}$$

For an arbitrary time dependent population, $P(x, t_1)$, the number of states leaving x_i for x_j is $T(x_i, x_j; t_1, t_2)P(x_i, t_1)$; from which it can be seen that the condition of detailed balance is directly related to the flow of the population at equilibrium. The consequence of a simulation not obeying detailed balance would then be that a system initially equilibrium could spontaneously leave equilibrium, contrary to the second law of thermodynamics.

Unfortunately the condition of detailed balance also dictates that the relative probability of transition to an important state (e.g., a transition state) x_i which has low equilibrium population density, $P_0(x_i)/P_0(x_j) \ll 1$, is very small. The simplest and most obvious method for sampling rare events without violating detailed balance is to perform a very large number of simulations; but for complex reactions which are compuationally intensive the number of additional trajectories required can be prohibitively large.

The idea behind the ensemble magnifying glass is to manipulate a simulation which began with a particular initial distribution, by incorporating additional trajectories at intermediate times cloned from trajectories of the previous distribution at instances when they are likely to transition to a rare event. In order to maintain detailed balance with cloning, each trajectory is assigned a statistical weight w_k starting at 1,

so that the time dependent population is

$$P(x,t) \approx \sum_k w_k \delta(x_k(t) - x), \tag{3.42}$$

When cloning occurs, the new trajectory, $x_{N+1}(t)$, is given a statistical weight $w_{N+1} = w_m/2$; and the weight of the original trajectory is changed from w_m to $w_m/2$. By manipulating the weights in this way, and not the dynamics of the motion, the population flux continues to satisfy the condition of detailed balance.

To verify that detailed balance is maintained, we consider transition rates with a stochastic intermediate cloning step. We can define the transition rate $T(x_2, x_1; t_2, t_1)$ by evolving a distribution which is initially a Dirac Delta Distribution:

$$T(x_2, x_1; t_2, t_1) = P_\delta(x_2, t_2) \tag{3.43}$$

if

$$P_\delta(x, t_1) = \delta(x - x_1). \tag{3.44}$$

To calculate $T(x_2, x_1; t_2, t_1)$ with an intermediate cloning step at time t', we evolve P_δ up until t' and then perform cloning. The population after cloning, P'_δ, is the sum of the two populations derived from the cloning, $P^{(1)}(x,t') = P^{(2)}(x,t') = \frac{1}{2}P_\delta(x,t')$:

$$P_\delta(x,t') \rightarrow P'_\delta(x,t') = P^{(1)}(x,t') + P^{(2)}(x,t') = P_\delta(x,t'). \tag{3.45}$$

The final population at t_2 determining the transition rate, is the sum of the cloned populations at t_2:

$$T(x_2, x_1; t_2, t_1) = P'_\delta(x_2, t_2) = P^{(1)}(x_2, t_2) + P^{(2)}(x_2, t_2) = P_\delta(x_2, t_2). \tag{3.46}$$

From which it is trivially clear that intermediate cloning steps do not affect the condition of detailed balance.

In order to choose when cloning should occur, we assume there is a function $f(x)$ which measures the proximity of a state to a rare event. States are then cloned with higher probability in accord with the degree of proximity to a rare event.

In the context of SuSy, the proximity function $f(x)$ is provided by the SuSy cloning and destroying rate, Equation 3.27. The compass vector in SuSyMD gives a statistical measure of the probability that the carrying trajectory will participate in a rare event corresponding to the transtion between metastable states. The result is a dynamically enhanced sampling of trajectories near the transition state, without affecting the physical realism of the evolved population distribution, and without any assumptions about the physics of the system besides the Hamiltonian.

For simplicity, we do not implement destroying with the ensemble magnifying glass, but the possibility of doing so is worth mentioning. In order to incorporate destroying, it is not enough to return the statistical weight to the cloned partner since doing so would be tantamount to a selective process which would violate detailed balance. We could imagine for instance using a proximity function which gave a definite probability for destroying trajectories when they left a region of configuration space. If the trajectory leaving the chosen region returned its statistical weight to the population inside the region, it would markedly enhance the length of time the population dwelled in the region without regard to the equilibrium population distribution. In order to preserve detailed balance in the context of destroying, statistical weight of the trajectories would need to be distributed to its nearest neighbors in configuration space in a way that minimizes the perturbation to the population distribution at the instance of destruction.

Normalization of SuSyMD population Density

Direct analysis of the density of the molecular dynamics phase space, (q, p), of a SuSyMD simulation incorporating cloning would not yield physically meaningful information about the associated population density equation density because of the violation of detailed balance described in Section 3.1.4.

This, violation can be seen directly from analysis of evolution of the joint distribution for the composite system in Equation 3.15. The effect of cloning on the

population on densities from the cloning rate given by 3.27 is to create a population density at (q,p) for the trajectories underlying the population in Equation 3.15 given by

$$P'(q,p,t) = \int |(\mathbf{u},\mathbf{w})|\, F(\mathbf{q},\mathbf{p},\mathbf{u},\mathbf{w})\, \mathrm{d}\mathbf{u}\ \mathrm{d}\mathbf{w}. \tag{3.47}$$

Substituting Equation 3.15 in to Equation 3.47 shows

$$\frac{\partial}{\partial t}P'(q,p,t) = \int |(\mathbf{u},\mathbf{w})| \frac{\partial F}{\partial t}\, \mathrm{d}\mathbf{u}\ \mathrm{d}\mathbf{w} \tag{3.48}$$

$$= \int -|(\mathbf{u},\mathbf{w})| \left(\mathbf{H}_{\mathrm{K}} + \sum_i \frac{\partial}{\partial u_i} w_i + \frac{\partial}{\partial w_i} \left(\gamma w_i + \frac{\partial^2 H}{\partial q_i \partial q_j}(\mathbf{q}) u_i \right) \right) F\, \mathrm{d}\mathbf{u}\ \mathrm{d}\mathbf{w} \tag{3.49}$$

$$= -\mathbf{H}_{\mathrm{K}} P' - \int |(\mathbf{u},\mathbf{w})| \sum_i \frac{\partial}{\partial u_i} w_i + \frac{\partial}{\partial w_i} \left(\gamma w_i + \frac{\partial^2 H}{\partial q_i \partial q_j}(\mathbf{q}) u_i \right) F\, \mathrm{d}\mathbf{u}\ \mathrm{d}\mathbf{w} \tag{3.50}$$

After integration by parts, this becomes

$$= -\mathbf{H}_{\mathrm{K}} P' + \int \left(\mathbf{u}\cdot\mathbf{w} + \gamma \mathbf{w}^2 + \mathbf{w}^T \mathbf{H} \mathbf{u} \right) \frac{F}{|(\mathbf{u},\mathbf{w})|}\, \mathrm{d}\mathbf{u}\ \mathrm{d}\mathbf{w}. \tag{3.51}$$

Which mathematical statement that the population P' does not obey the continuity relation implicit in the Kramer's equation due to the cloning and destroying accompanying diffusion in $\mathbf{u}$ and $\mathbf{w}$.

However, the normalized joint distribution, defined by

$$\tilde{F}(\mathbf{q},\mathbf{p},\mathbf{u},\mathbf{w}) = \frac{F(\mathbf{q},\mathbf{p},\mathbf{u},\mathbf{w})}{|(\mathbf{u},\mathbf{w})|}, \tag{3.52}$$

gives a population

$$P(q,p,t) = \int |(\mathbf{u},\mathbf{w})|\, \tilde{F}(\mathbf{q},\mathbf{p},\mathbf{u},\mathbf{w})\, \mathrm{d}\mathbf{u}\ \mathrm{d}\mathbf{w} \tag{3.53}$$

$$= \int F(\mathbf{q},\mathbf{p},\mathbf{u},\mathbf{w})\, \mathrm{d}\mathbf{u}\ \mathrm{d}\mathbf{w} \tag{3.54}$$

which does obey the Kramer's equation:

$$\frac{\partial}{\partial t}P(q,p,t) = \int |(\mathbf{u},\mathbf{w})| \frac{\partial \tilde{F}}{\partial t}\, \mathrm{d}\mathbf{u}\, \mathrm{d}\mathbf{w} \tag{3.55}$$

$$= \int \frac{\partial F}{\partial t}\, \mathrm{d}\mathbf{u}\, \mathrm{d}\mathbf{w} \tag{3.56}$$

$$= \int -\left(\mathbf{H}_{\mathrm{K}} + \sum_i \frac{\partial}{\partial u_i} w_i + \frac{\partial}{\partial w_i}\left(\gamma w_i + \frac{\partial^2 H}{\partial q_i \partial q_j}(\mathbf{q}) u_i\right)\right) F\, \mathrm{d}\mathbf{u}\, \mathrm{d}\mathbf{w} \tag{3.57}$$

$$= -\mathbf{H}_{\mathrm{K}} P - \int \sum_i \frac{\partial}{\partial u_i} w_i + \frac{\partial}{\partial w_i}\left(\gamma w_i + \frac{\partial^2 H}{\partial q_i \partial q_j}(\mathbf{q}) u_i\right) F\, \mathrm{d}\mathbf{u}\, \mathrm{d}\mathbf{w} \tag{3.58}$$

In this case the continuity relation for the compass density currents in Equation 3.13 gives a net zero divergence:

$$= -\mathbf{H}_{\mathrm{K}} P. \tag{3.59}$$

From the cloning rate in Equation 3.27, the number of cloning events, N_c, experienced by trajectories reaching the extended phase space point $(\mathbf{q}, \mathbf{p}, \mathbf{u}, \mathbf{w})$ is $N_c \approx \log_2 |(\mathbf{u}, \mathbf{w})|$. The number of trajectories created by the ensemble reaching this point is then 2^{N_c}. Giving the trajectories a statistical weight and population as in 3.42, produces a population

$$P(q,p,t) \approx \sum_k \frac{1}{2^{N_c}} \delta(q_k(t) - q)\delta(p_k(t) - p), \tag{3.60}$$

which is the approximation of the population in Equation 3.53,

$$P(q,p,t) = \int |(\mathbf{u},\mathbf{w})|\, \tilde{F}(\mathbf{q},\mathbf{p},\mathbf{u},\mathbf{w})\, \mathrm{d}\mathbf{u}\, \mathrm{d}\mathbf{w} \tag{3.61}$$

$$\tag{3.62}$$

Similarly, an unnormalized sum gives the sampling density in Equation 3.47:

$$P'(q,p,t) \approx \sum_k \delta(q_k(t) - q)\delta(p_k(t) - p,) \tag{3.63}$$

In the following examples, we consider the sampling populations from SuSy MD simulations.

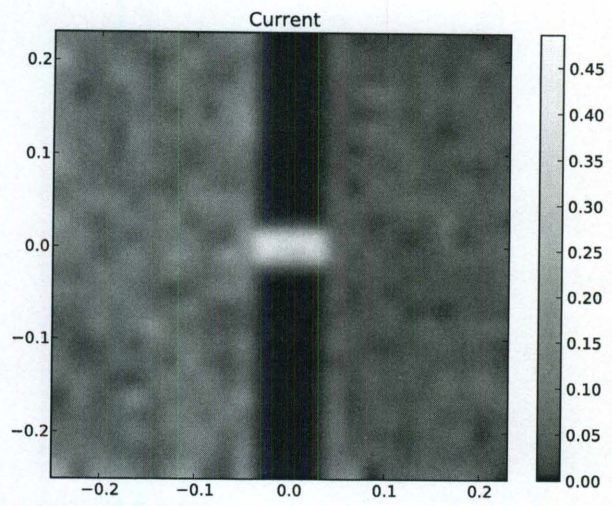

Figure 3.7 : In this purely entropic reaction system, the reactant barrier is clearly identified by the region of high current density.

3.1.5 Two dimensional SuSyMD examples

Purely Entropic Barrier

An example of a reaction barrier which is purely entropic, we create an energy profile like the one depicted in Figure 1.2. The system is characterized by a region of zero forces surrounded by perfect reflecting walls and a narrow passage way between two regions of large configuration volume. In this case, for the regions we described in Section 3.1.4, the compass vectors have a neglible impact on the trajectory population within the well. However, since there is no energy barrier, molecular dynamics simulations by themselves are able to easily form a a well sampled current density, dependent only on the rate at which particles find the narrow passage way. To demonstrate this, we simualated a system of this kind using a population of 100 000 trajectories. The current at each position in configuration space was calculated by taking the approximate average of J_{q_i} in Equation 1.9. The result is depicted in Figure 3.7.

Entropic and Energetic Barrier

Free energy barriers for chemical reactions are typically formed by both energetic and entropic limitations together due to the analytic functions giving energy profiles in real systems. In this section we present the results of simulations of a model system demonstrating the ability of SuSyMD to dramatically enhance sampling of the difficult to reach energy peak.

These simulations were conducted by creating an entropic barrier type system with an energy given by cubic spline interpolation to create a barrier height of $5kT$. The simulation was performed at a temperature of 0.6 in units of $kT = 1$. The initial population consisted of 1 000 trajectories in the well on the right hand side of the configuration space. Cloning was prohibited so that the population could be normalized to a population distribution obeying detailed balance in the diffusion as described in Section 3.1.4.

After simulating for 2 pico seconds, the SuSy population reached a population of 600 000 trajectories, with most of the population concentrated on the energetic barrier.

For comparison, we simulated 200 000 trajectories using normal MD for the same period of time and the same conditions. This number of trajetories was chosen due to the fact that it represented the same amount of simulation time as used in the SuSyMD simulation. It is important to note however, that SuSyMD scaled *itself* to the level necessary to observe barrier crossing. Even with this large number of trajectories used in the MD simulation, after 2 pico seconds, only 6 of the MD trajectories were able to cross the barrier. Furthermore, although only a small fraction of the total population distribution crossed the barrier in this time, the actual number of SuSyMD trajectories was on the order of 200, giving a much finer sampling of the distribution of product trajectories after barrier crossing.

While the primary focus of the SuSyMD simulations was achieved, namely enhancement of sampling in the relevant reaction barrier, the fraction of the relative

normalized population of trajectories which reacted according to the SuSy simulation disagreed with the MD simulation by 3 orders of magnitude (3×10^{-5} versus 1×10^{-8}). This error is attributed to the much smaller *attempt* rate by the initial population in the reactant well for the initial SuSy simulation. The requirement for an initial trajectory to attempt the barrier crossing in order to gain enhanced sampling is shown in detail in figures 3.12 through 3.22.

Figures 3.12 through 3.22 also demonstrate how the computational cost of the additional SuSyMD trajectory clones could be mitigated. The simulation shows that an overabundance of trajectories was produced due to acceleration in the *positive* curvature regions of the barrier. While these trajectories can not in general be removed without violating detailed balance, clones which cycle through positive curvature compass vector oscillations do so in a period of time so short that it should be possible to merge them with significant perturbation to detailed balance.

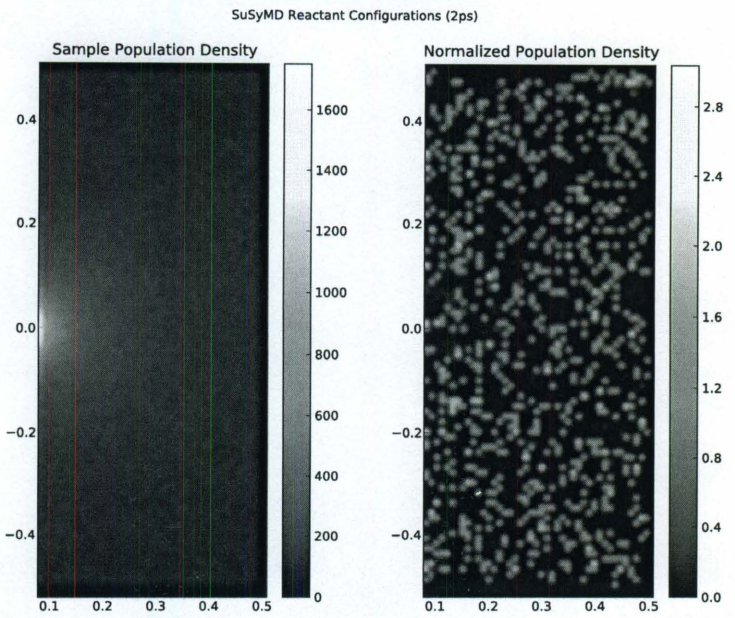

Figure 3.8 : This figure depicts the sampling and normalized SuSy population densities in the reactant well resulting from the 2ps simulation described in 3.1.5. In the left frame, the actual population of SuSy trajectories is displayed, showing the trajectories are concetrated on the barrier at the origin. On the right hand side, the populations have been statistically reweighted to give a normal Kramer's distribution, which evolves while observing detailed balanc.e

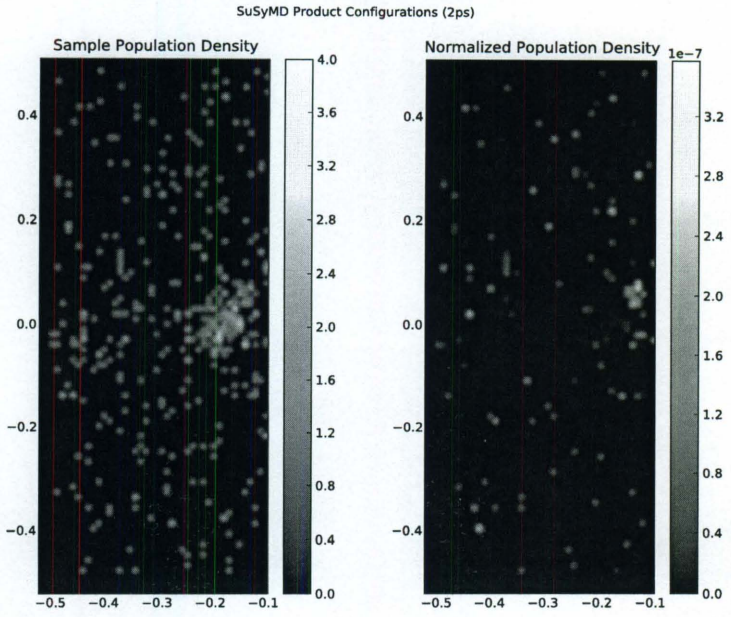

Figure 3.9 : This figure depicts the sampling and normalized SuSy population densities in the product well resulting from the 2ps simulation described in 3.1.5. The sampling population in the left frame shows that approximately 200 SuSy trajectories crossed the barriers, while the right frame shows that the statistically reweighted population correctly shows neglible barrier crossing.

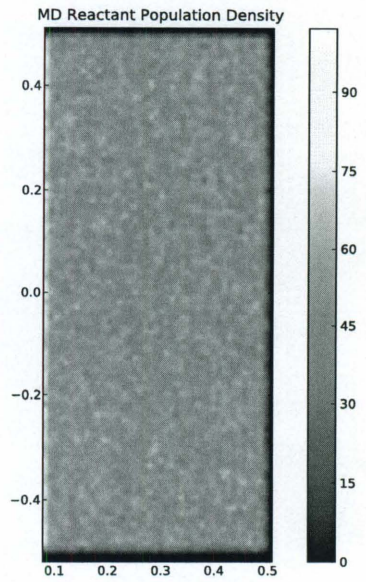

Figure 3.10 : This figure depicts the sampling and normalized SuSy population densities in the reactant well resulting from the 2ps simulation described in 3.1.5. Despite the enormous number of trajectories, only 6 reactants were able to cross the barrier at the origin during the simulation time.

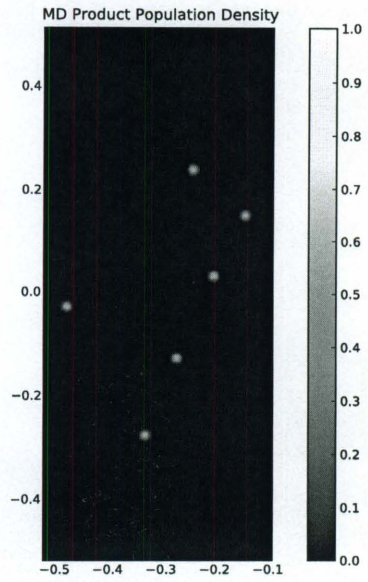

Figure 3.11 : This figure depicts the sampling and normalized SuSy population densities in the reactant well resulting from the 2ps simulation described in 3.1.5. It demonstrates that despite the enormous number of trajectories, only 6 reactants were able to cross the barrier at the origin during the simulation time.

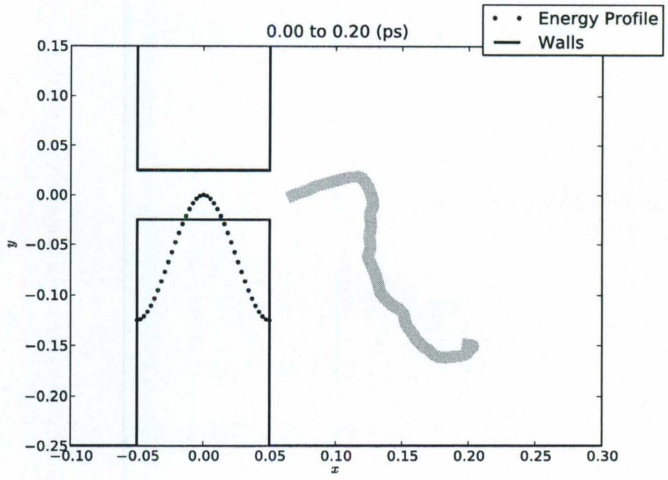

Figure 3.12 : The carrying trajectories for a SuSyMD simulation in a system with an energetic barrier at the origin for the time interval between 0 and 0.2 picoseconds. The simulations began with a single trajectory. The relative statistical weights are denoted by the line widths. Cloning events are denoted by red circles. The profile of the energy barrier along the x coordinate is provided (not to scale) for reference. The carrying trajectory is initially in a free particle region of flat energy, implicitly searching for a barrier. Without forces, the compass trajectory is stationary, and is not presented for brevity.

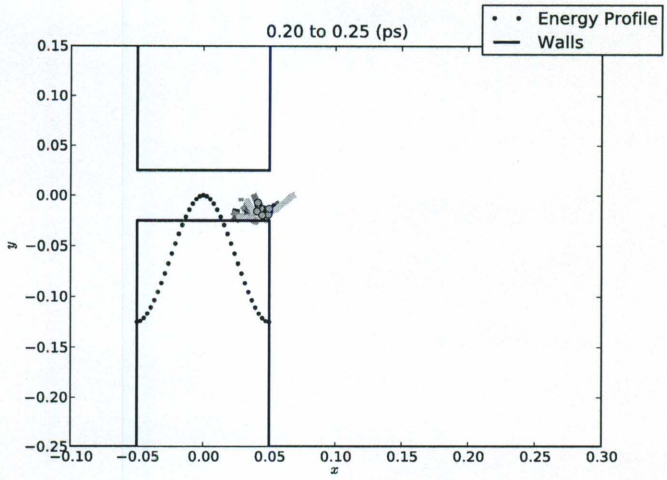

Figure 3.13 : The carrying trajectories for a SuSyMD simulation in a system with an energetic barrier at the origin for the time interval between 0.20 and 0.25 picoseconds. The simulations began with a single trajectory. The relative statistical weights are denoted by the line widths. Cloning events are denoted by red circles. The profile of the energy barrier along the x coordinate is provided (not to scale) for reference. 3.14 *Around 0.2 pico seconds, the trajectory collides with the energetic barrier. The rapid acceleration of the compass trajectory increases the compass vector magnitude leading to rapid cloning.*

3.2 Barrier resistance

The usual expression for reaction rate can be derived from the Fokker-Planck equation, [add ref], which is the divergence of the current operator, $\left(T\frac{\partial}{\partial x_i} + F_i\right)\psi(\mathbf{x}) = \mathbf{J}(\mathbf{x})$. The Fokker-Planck equation is not Hermitian, so right eigenstates are not left eigenstates. But left eigenstates can be derived from left eigenstates via a conjugation operator, $|\psi_L\rangle = R\,|\psi_R\rangle = \exp\{E/T\}\,|\psi_R\rangle$, so that if $\mathbf{H}_{\mathrm{FP}}\,|\psi_R\rangle = \lambda\,|\psi_R\rangle$, then $\langle\psi_L|\,\mathbf{H}_{\mathrm{FP}} = \langle\psi_R|\,\lambda$. And left and right eigenstates have a biorthonormality relation $\langle\psi_L\,|\psi_R\rangle = 1$.

Then, it follows that when ψ is the quasi-equilibrium population for an escaping

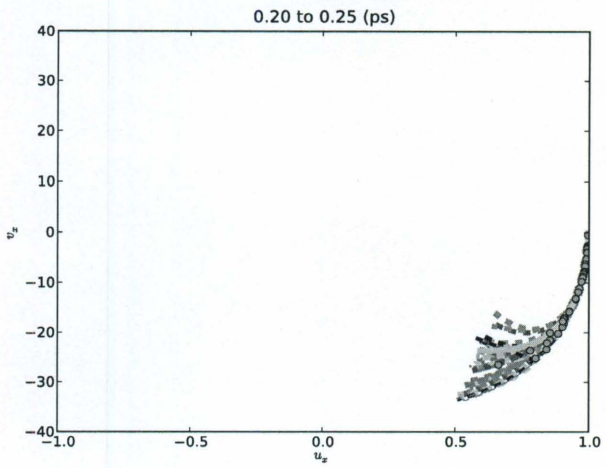

Figure 3.14 : The phase space trajectory for the compass trajectory of a SuSyMD simulation in a system with an energetic barrier for the time interval between 0.2 and 0.25 picoseconds. The carrying tajectory is depicted in Figure 3.13. *Around 0.2 pico seconds, the trajectory collides with the energetic barrier. The rapid acceleration of the compass trajectory increases the compass vector magnitude leading to rapid cloning.*

current,

$$\lambda \langle \psi_L(t) \, | \psi_R(t) \rangle = \langle \psi_L \, | \mathbf{H}_{\mathrm{FP}} | \, \psi_R \rangle \tag{3.64}$$

$$= \left\langle \psi_L \left| \frac{\partial}{\partial x_i} \left(T \frac{\partial}{\partial x_i} + F_i \right) \right| \psi_R \right\rangle \tag{3.65}$$

$$= \left\langle \psi_R \left| \exp\{E/T\} \frac{\partial}{\partial x_i} \left(T \frac{\partial}{\partial x_i} + F_i \right) \right| \psi_R \right\rangle \tag{3.66}$$

$$= \left\langle \psi_R \left| \left(T \frac{\partial}{\partial x_i} + F_i \right)^{\dagger} \exp\{E/T\} \left(T \frac{\partial}{\partial x_i} + F_i \right) \right| \psi_R \right\rangle \tag{3.67}$$

$$= \langle \mathbf{J}_R \, | \exp\{E/T\} | \, \mathbf{J}_R \rangle \tag{3.68}$$

$$= \int \exp\{E/T\} \, [\mathbf{J}(\mathbf{x})]^2 \, \mathrm{d}\mathbf{x}. \tag{3.69}$$

Dividing by the total population, $\langle \psi_L(t) \, | \psi_R(t) \rangle$ gives the relaxation rate for the reaction. The resulting expression,

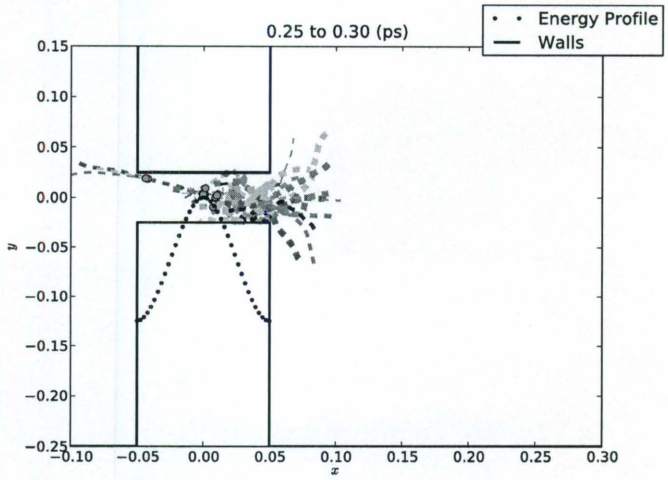

Figure 3.15 : The carrying trajectories for a SuSyMD simulation in a system with an energetic barrier at the origin for the time interval between 0.25 and 0.3 picoseconds. The simulations began with a single trajectory. The relative statistical weights are denoted by the line widths. Cloning events are denoted by red circles. The profile of the energy barrier along the x coordinate is provided (not to scale) for reference. 3.16 *After the initial impact on the barrier around 0.2 picoseconds, the trajectories which remain in the positive curvature region terminate cloning, whereas the few trajectories continuing into the negative curvature region experience additional cloning.*

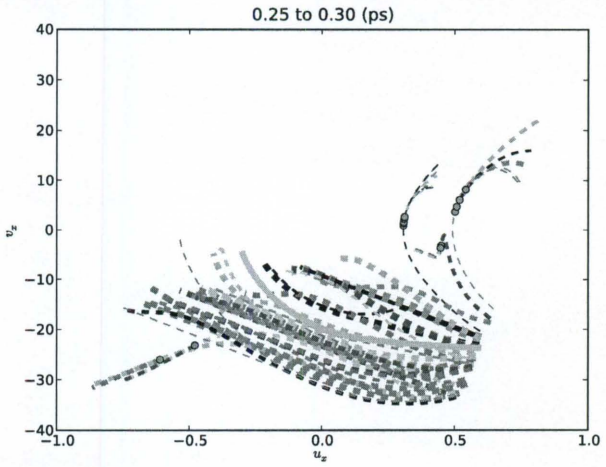

Figure 3.16 : The phase space trajectory for the compass trajectory of a SuSyMD simulation in a system with an energetic barrier for the time interval between 0.25 and 0.3 picoseconds. The carrying tajectory is depicted in Figure 3.15. *After the initial impact on the barrier around 0.2 picoseconds, the trajectories which remain the positive curvature region terminate cloning, whereas the few trajectories continuing into the negative curvature region experience additional cloning. Ideally, the trajectories moving towards the origin of the compass phase space would be destroyed, however since we wish avoid to perturbing detailed balance (as discussced in Section 3.1.4), we refrain from removing trajectories and the excess trajectories remain in the simulation.*

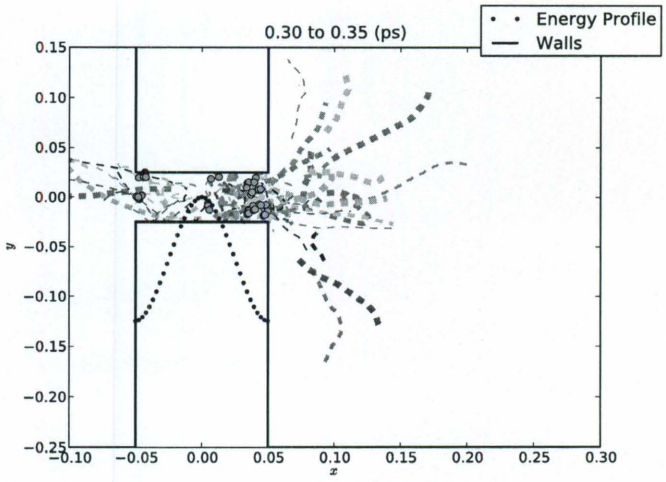

Figure 3.17 : The carrying trajectories for a SuSyMD simulation in a system with an energetic barrier at the origin for the time interval between 0.3 and 0.35 picoseconds. The simulations began with a single trajectory. The relative statistical weights are denoted by the line widths. Cloning events are denoted by red circles. The profile of the energy barrier along the x coordinate is provided (not to scale) for reference. 3.18 *The trajetoies which remained in the positive cloning region have begun to enter the second half of the period of harmonic motion and experience additional cloning from the acceleration of the compass vetor in the reverse direction. The trajectories in the negative curvature region experience rapid additional cloning due to steady acceleration of the compass vector; this increases the likelihood of finding trajectories which remain at the barrier peak.*

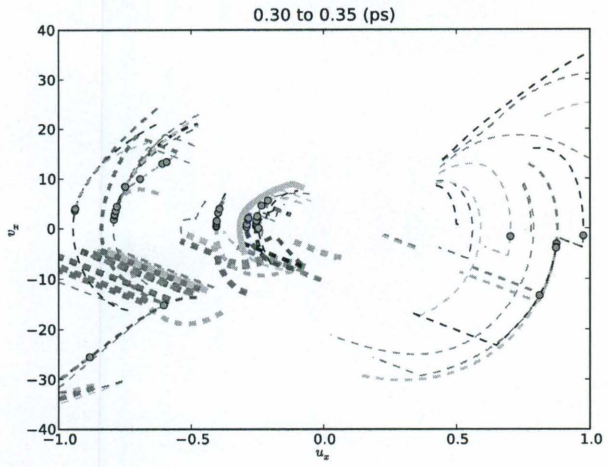

Figure 3.18 : The phase space trajectory for the compass trajectory of a SuSyMD simulation in a system with an energetic barrier for the time interval between 0.3 and 0.35 picoseconds. The carrying tajectory is depicted in Figure 3.17. *The trajectories which remained in the positive cloning region have begun to enter the second half of the period of harmonic motion and experience additional cloning from the acceleration of the compass vetor in the reverse direction. The trajectories which have returned to the free particle region experience a near linear descent to zero velocity in the compass vector phase space. The trajectories in the negative curvature region continue to experience rapid additional cloning due to steady acceleration of the compass vector.*

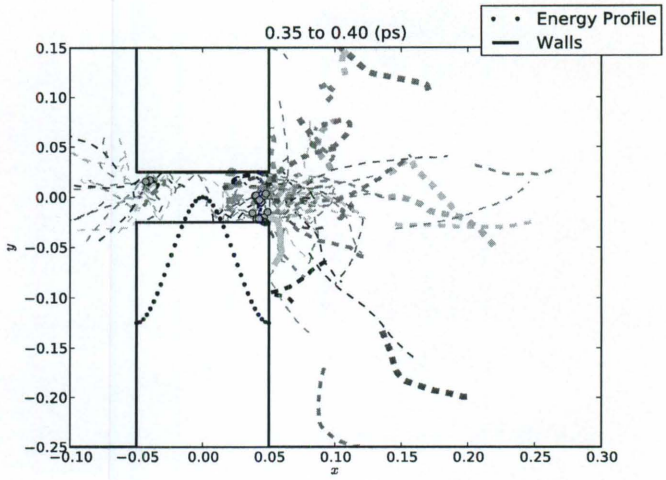

Figure 3.19 : The carrying trajectories for a SuSyMD simulation in a system with an energetic barrier at the origin for the time interval between 0.35 and 0.4 picoseconds. The simulations began with a single trajectory. The relative statistical weights are denoted by the line widths. Cloning events are denoted by red circles. The profile of the energy barrier along the x coordinate is provided (not to scale) for reference. 3.20 *Most of the trajectories which remained in the positive curvature region begin their exit from the barrier region, and cloning of trajectories in the negative curvature region at the barrier peak continues; this increases the likelihood of finding trajectories which remain at the barrier peak.*

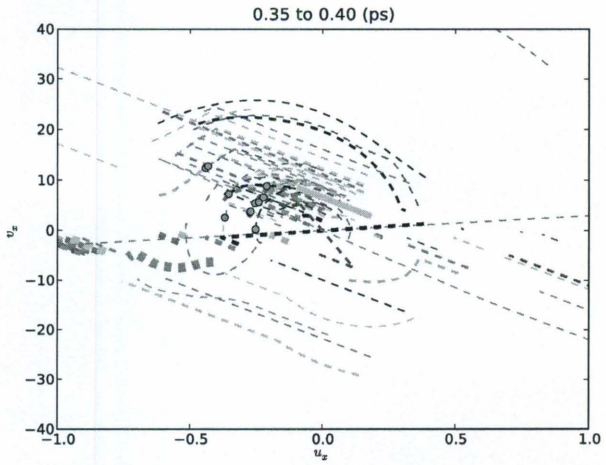

Figure 3.20 : The phase space trajectory for the compass trajectory of a SuSyMD simulation in a system with an energetic barrier for the time interval between 0.35 and 0.4 picoseconds. The carrying tajectory is depicted in Figure 3.19. *The few trajectories which have remained in the positive curvature region continue to the peak of their phase space oscillation. The trajectories in the negative curvature region have left the scope of the phase space region depicted, but continue to be rapidly cloned. We begin to see trajectories which* appear *to cross the origin in the compass phase space due to reflection from the barrier walls.*

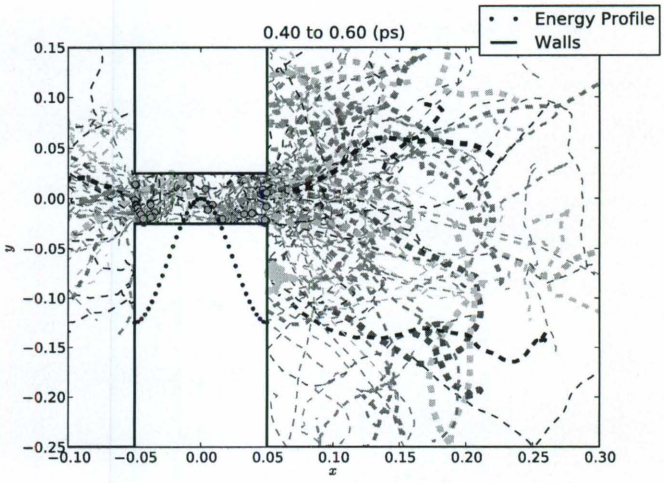

Figure 3.21 : The carrying trajectories for a SuSyMD simulation in a system with an energetic barrier at the origin for the time interval between 0.4 and 0.6 picoseconds. The simulations began with a single trajectory. The relative statistical weights are denoted by the line widths. Cloning events are denoted by red circles. The profile of the energy barrier along the x coordinate is provided (not to scale) for reference. 3.20 *Most of the trajectories have left the barrier region, but the few that remain in both the positive and negative curvature regions experience continued cloning.*

$$\lambda = \frac{\int \exp\{E/T\}\,[\mathbf{J}(\mathbf{x})]^2\,\mathrm{d}\mathbf{x}}{\int \exp\{E/T\}\,\psi^2\,\mathrm{d}\mathbf{x}} \tag{3.70}$$

can be seen as a generalized Kramer's escape rate (Equation 1.28). In the quasi-equilibrium approximation, we may write the population as $\psi \approx e^{-E/T}$, so that the denominator is

$$\int \exp\{E/T\}\,\psi^2\,\mathrm{d}\mathbf{x} \approx \int \psi\,\mathrm{d}\mathbf{x} = p \tag{3.71}$$

so that we see the configurations which maximize the integrand in the numerator are the regions which contribute most to the Kramer's escape. The integrand was identified by Kurchan[15, 14], and is termed the barrier resistance

$$J_B = \exp\{E/T\}\,[\mathbf{J}(\mathbf{x})]^2. \tag{3.72}$$

Moreover, the expression in Equation 3.70 is exact, whereas the Kramer's escape integral is only an approximation.

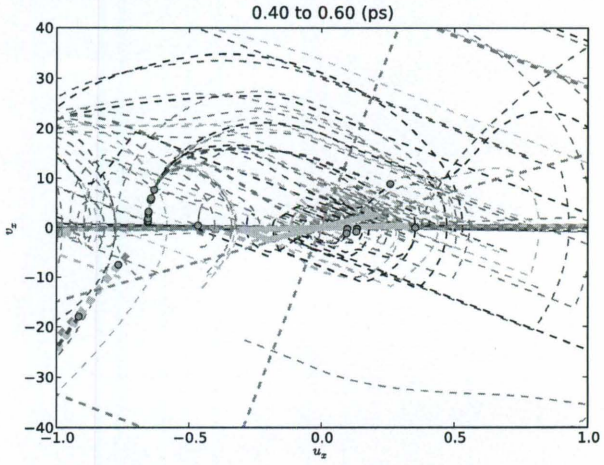

Figure 3.22 : The phase space trajectory for the compass trajectory of a SuSyMD simulation in a system with an energetic barrier for the time interval between 0.4 and 0.6 picoseconds. The carrying tajectory is depicted in Figure 3.21. *Most of the trajectories have left the barrier region and evince near linear motion in the compass phase space as they decay to zero velocity. The few trajectories that remained in both the positive and negative curvature regions experience continued cloning. The trajectories which give apparent rapid motion across the origin are the result of reflections from the barrier walls.*

Finding the regions which contribute the most to relaxation times is then a matter of finding the regions in configuration space with the dominant barrier resistance. In the case where there are multiple strongly contributing regions to the transition rate, the barrier resistance would identify all of them, and the degree of their contribution to the escape rate.

The barrier rate integral, and hence the relaxation rate can be calculated directly from a simulated population. To do this, we rewrite the barrier resistance as

$$J_B(\mathbf{x}) = \exp\{E(\mathbf{x})/T\}\,[\mathbf{J}(\mathbf{x})]^2 = \exp\{-E(\mathbf{x})/T\}\,|\nabla(\exp\{E(\mathbf{x})/T\}\,\psi)|^2\,. \tag{3.73}$$

In terms of the population from Equation 3.60, we write

$$\exp\{E(\mathbf{x})/T\}\,\psi(\mathbf{x}) \approx \exp\{E(\mathbf{x})/T\} \sum_k \frac{1}{2^{N_c}} \delta(\mathbf{x}_k(t) - \mathbf{x}) \tag{3.74}$$

$$\tag{3.75}$$

so that the gradient can be approximated by

$$\nabla\left(\exp\{E(\mathbf{x})/T\}\,\psi(\mathbf{x})\right) \tag{3.76}$$

$$\approx \exp\{E(\mathbf{x})/T\}\left(\beta\nabla E(\mathbf{x}) \sum_k \frac{1}{2^{N_c}} \delta(\mathbf{x}_k(t) - \mathbf{x}) + \sum_k \frac{1}{2^{N_c}} \nabla\delta(\mathbf{x}_k(t) - \mathbf{x})\right). \tag{3.77}$$

So that the integrand in Equation 3.73 is

$$J_B(\mathbf{x}) \approx \exp\{E(\mathbf{x})/T\} \left|\beta\nabla E(\mathbf{x}) \sum_k \frac{1}{2^{N_c}} \delta(\mathbf{x}_k(t) - \mathbf{x}) + \sum_k \frac{1}{2^{N_c}} \nabla\delta(\mathbf{x}_k(t) - \mathbf{x})\right|^2 . \tag{3.78}$$

The computational cost of the sum over the trajectories, $\sum_k$, is be reduced by making use of the fact that the histogram basis δ is non-zero only when $\mathbf{x}_k \approx \mathbf{x}$; the sum for the estimation of $J_B(\mathbf{x})$ need only involve nearest neighbors. The nearest neighbors for the calculation, and hence the entire calculation of $J_B(\mathbf{x})$, can be found rapidly and massively in parallel using algorithms such as the Geometric Neighbor Acess Tree[1].

The integral for $\int J_B(\mathbf{x})\,\mathrm{d}\mathbf{x}$, and discretely sampled integrands in general, are approximated by a sum of the form

$$\int J_B(\mathbf{x})\,\mathrm{d}\mathbf{x} \approx \sum_k (\Delta\mathbf{x})_k^{3N} J_B(\mathbf{x}_k), \tag{3.79}$$

where the step size $(\Delta\mathbf{x})_k^n$ is effectively the weight associated with a discrete point for accurate approximation of the integral. The appropriate step size can be determined by Gaussian interpolation as in Equation 2.28. The approximation of the integral is then

$$\int J_B(\mathbf{x})\,\mathrm{d}\mathbf{x} \approx \int \sum_k c_k G\left(\alpha_k, \mu_k; x\right)\,\mathrm{d}\mathbf{x} \tag{3.80}$$

$$= \sum_k \left(\frac{2\pi}{a}\right)^{3N/2} c_k, \tag{3.81}$$

where we identify $(\Delta\mathbf{x})_k^{3N} = \left(\frac{2\pi}{a}\right)^{3N/2} c_k / J_B(\mathbf{x}_k)$. The linear interpolation equation, Equation 2.29, also need only involve nearest neighbors.

Combining the integral approximation in Equation 3.79 with accurate sampling near the transition state derived from SuSyMD will then provide a direct means to calculate reaction rates without the concern for recrossing issues or coordinate system distortions.

Chapter 4

Conclusion

One of the most important problems facing the study of complex chemical systems such as proteins is the location and accurate characterization of the limiting steps in the reactions. In the introduction, we described in detail many of the underyling challenges making this task a difficult issue.

In response to these issues, we have propopsed a definition of a transition state for complex reactions, the χ_1 separatrix in Part 2, which, when accurately identified, can be used to calculate relaxation rates directly instead of upper bounds for one way reaction rates. Because calculation of reaction rates when using this separatrix can be done without traversing most of the configuration space, location of this barrier either by experimental or theoretical means would drastically reduce the simulation time required for theoretical reaction rate predictions.

The theory behind χ_1 separatrix also justifies the use of SuSyMD for locating the regions most relevant to calculation of reaction times. Because the χ_1 separatrix is the surface of largest current flux during a reaction, and the SuSyMD method automatically scales the population size and anneals the sampling population to regions of large current density on the intermediate timescale $t \sim 1/\lambda_2$, it provides a simple scheme for automatic location and exploration of the energetic and entropic barriers inherent most relevant to the relaxation rate.

References

[1] S. Brin. Near neighbor search in large metric spaces. In *21th International Conference on Very Large Data Bases*, 1995.

[2] Joseph D. Bryngelson and Peter G. Wolynes. Intermediates and barrier crossing in a random energy model (with applications to protein folding). *The Journal of Physical Chemistry*, 93(19):6902–6915, September 1989.

[3] Samuel S Cho, Yaakov Levy, and Peter G Wolynes. P versus Q: structural reaction coordinates capture protein folding on smooth landscapes. *Proceedings of the National Academy of Sciences of the United States of America*, 103(3):586–91, January 2006.

[4] C Clementi, H Nymeyer, and J N Onuchic. Topological and energetic factors: what determines the structural details of the transition state ensemble and "en-route" intermediates for protein folding? An investigation for small globular proteins. *Journal of molecular biology*, 298(5):937–53, 2000.

[5] Aaron R Dinner. Automatic Method for Identifying Reaction Coordinates in Complex Systems. *Society*, pages 6769–6779, 2005.

[6] Rose Du, Vijay S Pande, and Eugene S Shakhnovich. On the transition coordinate for protein folding. *Journal of Chemical Physics*, 108(1):334–350, 1998.

[7] W E, W Ren, and E Vandeneijnden. Transition pathways in complex systems: Reaction coordinates, isocommittor surfaces, and transition tubes. *Chemical Physics Letters*, 413(1-3):242–247, 2005.

[8] Peter Hänggi, Peter Talkner, and Michal Borkovec. Reaction-rate theory: fifty years after kramers. *Rev. Mod. Phys.*, 62(2):251–341, Apr 1990.

[9] Hans Frauenfelder and Peter G. Wolynes. Rate Theories and Puzzles of Hemeprotein Kinetics. *Advancement Of Science*, 229(4711):337–345, 1985.

[10] Graeme Henkelman, Gisli Johannesson, and Hannes Jonnson. Methods for Finding Saddle Points and Minimum Energy Paths. *Progress on Theoretical Chemistry and Physics*, pages 269–300, 2000.

[11] Lei Huang and Dmitrii E Makarov. The rate constant of polymer reversal inside a pore. *The Journal of chemical physics*, 128(11):114903, 2008.

[12] James C. Keck. Variational Theory of Chemical Reaction Rates Applied to Three-Body Recombinations*. *Chemical Physics*, 32(4), 1960.

[13] H A Kramers. Brownian Motion in a Field of Force and The Diffusion Model of Chemical Reactions. *Physica*, VII(4):284–304, 1940.

[14] Jorge Kurchan. Metastable States, Transitions, Basins and Borders at Finite Temperatures. *Journal of Statistical Physics*, 116(5):1201–1245, 2004.

[15] Jorge Kurchan and Sorin Ta. Topological Methods for Searching Barriers and Reaction Paths . *October*, 91(18):1–4, 2003.

[16] R. Mannella. Quasisymplectic integrators for stochastic differential equations. *Physical Review E*, 69(4), 2004.

[17] Alessandro Mossa and Cecilia Clementi. Supersymmetric Langevin Equation to Explore Free-Energy Landscapes. *Physical Review E*, 75:046707, 2007.

[18] Eli Pollak and Peter Talkner. Reaction rate theory: what it was, where is it today, and where is it going? *Chaos*, 15(2):26116, 2005.

[19] H. Risken. *The Fokker-Planck Equation: Methods of Solution and Applications.* Springer-Verlag, 1984.

[20] Julien Tailleur and Jorge Kurchan. Kramers Equation and Supersymmetry. *Journal of Statistical Physics*, 122(4):557–595, 2006.

[21] David J. Wales. *Energy Landscapes With Applications to Clusters, Biomolecules and Glasses.* Press Syndicate fo the University of Cambridge, 2003.

[22] E. Wigner. The Transition State Method. *Journal of Chemical Physics*, 5(720):29–41, 1937.

[23] Eugene Wigner and Henry Eyring. On the Rate of Chemical Reactions. *The Scientific Monthly*, 44(6):564 – 567, 1937.